

## Article

# Non-Destructive Estimation of Moisture Percentage in Fired Red Brick Using Digital Image Processing and Artificial Intelligence

Andrés Pech-Pérez <sup>1,2,\*</sup>, Aida Alejandra Ricárdez-Montiel <sup>2</sup> and Aida Andrea Pech-Ricárdez <sup>3</sup>

- <sup>1</sup> Instituto Tecnológico de Oaxaca, Avenida Ingeniero Víctor Bravo Ahuja 125, Esquina Calzada Tecnológico, Oaxaca de Juárez 68030, Oaxaca, Mexico
- <sup>2</sup> Smart Ray Geosolutions, Privada de Rosales 107, Colonia Reforma, Oaxaca de Juárez 68050, Oaxaca, Mexico; andrespech@yahoo.com
- <sup>3</sup> Independent Visual Artist, Privada de Rosales 107, Colonia Reforma, Oaxaca de Juárez 68050, Oaxaca, Mexico; aidapech97@gmail.com
- \* Correspondence: andres.pp@itoaxaca.edu.mx

**Abstract:** In this study, we present a novel methodology for reducing uncertainties in detecting high-permeability regions in bricks by integrating brick imagery, color theory, unsupervised learning, and petrophysical concepts. Leveraging smartphone technology, our methodology identifies and analyzes moisture regions in red bricks, demonstrating its potential as a cost-effective tool for moisture characterization. This approach complements specialized moisture detection devices, highlighting the versatility of existing technology. Applied within the context of traditional red brick manufacturing in San Agustín Yatareni, Oaxaca, México, our results show that this methodology effectively identifies moisture-related anomalies, with water absorption values verified according to the NMX-C-404-ONNCCE-2012 and NMX-C-037-ONNCCE-2013 Mexican standards. We observed a significant inverse correlation between luminosity and moisture content, and a direct correlation between hue and moisture content. These findings suggest a reliable, non-invasive indicator of moisture levels, potentially improving the longevity of construction materials. The broader applicability of this approach in construction material analysis, particularly for bricks incorporating organic fibers, underscores its value as a tool for quality control. Furthermore, the integration of smartphone technology and interdisciplinary techniques contributes to advancing sustainable construction practices and improving material durability.



Received: 4 November 2024  
Revised: 11 January 2025  
Accepted: 14 January 2025  
Published: 1 February 2025

**Citation:** Pech-Pérez, A.; Ricárdez-Montiel, A.A.; Pech-Ricárdez, A.A. Non-Destructive Estimation of Moisture Percentage in Fired Red Brick Using Digital Image Processing and Artificial Intelligence. *Constr. Mater.* **2025**, *5*, 7. <https://doi.org/10.3390/constrmater5010007>

**Copyright:** © 2025 by the authors. Licensee MDPI, Basel, Switzerland. This article is an open access article distributed under the terms and conditions of the Creative Commons Attribution (CC BY) license (<https://creativecommons.org/licenses/by/4.0/>).

**Keywords:** smartphone technology; color formats; image processing; fired red brick; unsupervised learning

## 1. Introduction

The challenge of understanding how brick properties change in the presence of moisture necessitates the use of advanced quantitative interpretation techniques, which should be integrated with geophysical and petrophysical methods. In this paper, we introduce an innovative interdisciplinary approach to identify high-permeability bricks, demonstrating that moisture percentage can be inferred from the combined utilization of brick images obtained with smartphones, color theory, color formats, unsupervised learning, and the fluid distribution above the free water level [1]. Our findings reveal that bricks with anomalously high permeability show significant variations in the bulk volume of water (BVW) when compared to conventional bricks. We emphasize the importance of linking moisture content, or bulk volume of water (BVW) values, with water saturation ( $S_w$ ). The key to

understanding permeability lies in the pore structure, wherein capillary-bound water, represented by BVW, is typically found in the pores. BVW quantifies the pore geometry, which is influenced by the size, shape, and arrangement of grains, thereby relating it to both permeability and porosity [1]. As mentioned before, highly permeable bricks are characterized by a notably lower moisture content or BVW.

Brick is one of the oldest and most influential building materials in history, originating over 6000 years ago in ancient Mesopotamia [2]. Initially made from sun-dried mud, bricks evolved with the introduction of kiln firing by civilizations such as the Sumerians, Babylonians, and Egyptians, which enhanced their durability [2]. The Romans further advanced brickmaking, using fired clay bricks to construct some structures [2]. In Mesoamerica, the Mayans used red bricks in the construction of pyramids, such as those in Comalcalco, a key trading port with significant architectural developments [3]. Throughout the Middle Ages, brick was integral to the construction of cathedrals, castles, and urban infrastructure in Europe, contributing to the distinct Gothic architectural style. In the Modern Age, bricks were used extensively in Northern European architecture and Georgian England [2]. Today, brick remains a versatile and durable material in contemporary architecture, valued for its strength and aesthetic appeal [4,5].

Fired red brick is a cornerstone of construction globally, prized for its durability and versatility. However, its performance can be significantly compromised by moisture within its structure. Moisture can degrade mechanical strength, promote mold formation, and reduce thermal insulation, ultimately affecting the integrity of buildings [6]. Fired clay ceramics exhibit long-term moisture-induced expansion due to a slow chemical reaction with atmospheric water [7]. This expansion, though it decreases over time, is significant and often underestimated. Early recognition of moisture expansion as a cause of cracking in brickwork was delayed, likely because older masonry used soft lime mortars [8]. This expansion is driven by the slow diffusion of water within the solid phases of the ceramic matrix [7]. This moisture expansion is directly linked to mass gain. While accelerated by high-temperature steaming, the expansion progresses slowly under normal atmospheric conditions, underscoring the persistent risk of cracking in brick structures over time [7]. Various studies have shown that temperature and moisture content are critical factors influencing the thermal conductivity of insulating materials [9]. Specifically, moisture transfer in building envelopes significantly impacts heat transfer processes, especially in hot and humid areas [9]. These studies highlight the issue that the thermal conductivity of commonly used insulation materials increases with rising temperature and humidity, underscoring moisture as a critical issue in bioclimatic structures [9].

Eco-friendly bricks, particularly those containing bagasse fibers, may face challenges in the future regarding biological degradation. This study introduces a methodology that can assist in performing quality control for bricks that incorporate organic fibers. The inclusion of organic materials in construction materials aims to enhance their sustainability and mechanical properties [10]. However, these fibers can introduce vulnerability to microbial attack, particularly in humid environments. Different investigations have been conducted to evaluate the growth of microorganisms on construction materials containing various percentages of organic fibers [10]. Although the firing process reduces organic matter, residual fibers can still pose a risk of biological degradation. Due to the amount of organic matter, this firing process could also increase the number and size of voids in the bricks. Long-term exposure to moisture may compromise the durability and structural integrity of eco-friendly building materials. Further research is needed to understand the influence of moisture on eco-friendly bricks, particularly those containing organic fibers [11]. Considering that moisture can lead to biological degradation in eco-friendly bricks, it is crucial to assess whether their heightened porosity and water absorption could

accelerate this process, potentially compromising their structural integrity over time [11]. The short-term improvements in compressive strength and bending resistance [10] might not translate into long-term durability, especially if the bricks are more susceptible to moisture-related issues due to increased porosity. Bricks that contain organic fibers have demonstrated low performance in capillarity tests [11]. This is crucial for eco-friendly bricks, where maintaining structural integrity over time is a key concern, especially in the context of climate change and increased seismic activity. As climate change intensifies weather patterns and moisture exposure, and as earthquakes become more frequent or severe, the durability of these bricks must be rigorously assessed to ensure their long-term performance in increasingly unpredictable environments. In the specialized literature, there is also a lack of information about the scalability of eco-friendly bricks and the potential challenges in maintaining consistent quality when applied to larger construction projects, such as the associated infrastructure required for the development of the Interoceanic Corridor. This is a major infrastructure project in México aimed at creating a trade and logistics route between the Atlantic and Pacific Oceans.

The non-destructive evaluation of moisture content in fired red bricks is crucial for ensuring the safety of structures. Traditional moisture measurement techniques, like drilling, are intrusive and costly, limiting their application in construction and conservation. Approaches that rely on a single non-destructive method often result in limited accuracy [12]. However, recent advancements have demonstrated that a more accurate quantitative assessment of moisture content in saline brick walls can be achieved using a combination of machine learning and two complementary non-destructive methods [12]. The cost of inadequate moisture management can be substantial, leading to millions of dollars in damages, structural repairs, downtime, and long-term operational costs. According to the United States Environmental Protection Agency [6], proper moisture management is essential to avoid significant costs, emphasizing the need for effective moisture control measures from the outset of construction projects.

Digital image processing presents a promising solution for non-invasively estimating the moisture content in fired red bricks. By capturing high-resolution images and analyzing them with advanced algorithms, it could be possible to detect and quantify moisture economically and effectively. Despite its potential, there is a scarcity of studies on this approach, and no established methodology exists for using digital image processing to estimate the moisture percentage or identify patterns associated with fractures and moisture levels in bricks. In the current digital era, process automation is vital for efficiency and competitiveness across various sectors. Unsupervised learning, a branch of artificial intelligence, allows machines to learn from data without human supervision, making it a powerful tool for automating imaging processes in the construction industry [13,14]. Identifying the hidden patterns in images of construction materials can help architects and engineers develop more effective bioclimatic strategies and create waterproof materials tailored to specific needs [6].

Photographing large areas for purposes such as structural inspection poses technical and logistical challenges. Achieving complete coverage, coordinating multiple cameras, and managing large volumes of data are significant obstacles. While unmanned aerial vehicles (UAVs) equipped with infrared cameras are used in various fields, their integration into the construction sector remains limited [15]. Ensuring image quality under varying lighting and weather conditions further complicates this task [16].

Building upon these longstanding challenges, our study seeks to integrate modern digital and AI-driven methodologies to address the impact of moisture on fired red brick, particularly in traditional settings. This study hypothesizes that applying digital image processing techniques, combined with artificial intelligence algorithms, can develop a

reliable methodology to estimate moisture percentage and detect fractures in fired red bricks non-destructively. This approach aims to provide the construction industry with an effective tool for material evaluation and quality control, thereby enhancing efficiency and sustainability in building projects.

In this context, our research offers a methodology that combines digital image analysis with AI techniques to deliver non-destructive moisture estimates. The primary objective of this study is to address critical knowledge gaps by adapting methodologies from industries like the energy sector, where digital image processing is extensively utilized to estimate moisture content in soils and crops [17] and to detect fractures [18]. By leveraging these techniques, this research identifies the visual characteristics and specific patterns related to moisture levels and fracturing in captured images. The findings could have practical applications in construction and building conservation, offering innovative, non-invasive tools for assessing material integrity. This interdisciplinary approach could not only enhance current practices but also contribute to the sustainability and resilience of construction materials.

## 2. Production of Fired Red Bricks in San Agustín Yatareni, Oaxaca, México

San Agustín Yatareni, located in the Central Valley of Oaxaca (see Figure 1) and approximately 5 km from the state capital, is renowned for its traditional production of artisanal fired red bricks. Bordered by San Andrés Huayapam to the north, Oaxaca de Juárez to the west, Tlaxiaco de Cabrera to the east, and Santa Lucía del Camino and San Sebastián Tutla to the south, this municipality has cultivated a brick-making tradition deeply embedded in its culture and economy for generations. The following description of the brick-manufacturing process is based on interviews conducted with local artisans.

- Clay extraction: the process begins with the extraction of clay from natural deposits (quarries) in the San Agustín Yatareni area. The local soil type, pellic vertisol, is characterized by high plasticity and significant expansion when wet, and by contraction when dry. Pellic vertisols are often darker than other vertisols, usually being black or very dark brown due to the high organic matter content or specific mineral compositions. This clay is ideal for brick production. The tradition of brickmaking in this area dates back to the 1960s.
- Clay preparation: the preparation of clay for brick production includes impurity removal through crushing, maturation via solar and air exposure, and sieving to achieve uniform granulometry. To produce a batch of 500 bricks, the clay is combined with water, sawdust, yellow soil, black soil, and yocuela to attain the desired plasticity. The resulting mortar is then allowed to rest for two days to ensure uniform consistency before molding.
- Molding: the mortar is hand-molded into bricks using traditional wooden molds called marks. This process involves pressing and compacting the mortar to form the characteristic rectangular and elongated shape. The molds are cleaned and sanded after every eight bricks are formed to ensure consistent quality.
- Outdoor drying: this stage is critical to the quality of newly molded bricks, as it ensures moisture removal and enhances their solidity and stability. The bricks are initially sun-dried outdoors for three to eight days and then moved to covered drying areas, where natural factors such as sunlight, wind, and humidity continue to influence the drying process.
- Firing in kilns: after outdoor drying, the bricks are fired in kilns with capacities of 500 to 1000 pieces, reaching temperatures up to 1000 °C, typically fueled by sawdust. The firing process, lasting 8 to 36 h depending on the kiln type and conditions, involves

continuous temperature fluctuations. This delicate stage hardens the bricks, imparts their characteristic red color, and may cause variations in color and shape due to fire dynamics.

- **Cooling and storage:** after cooling in the kiln for up to eight days, the bricks are removed and stored for sale or for use in construction. Traditional fired red bricks typically measure  $5 \times 13 \times 26$  cm or  $5 \times 13 \times 27$  cm, with slight variations arising from the wooden molds, which measure  $5.3 \times 14 \times 28$  cm. In construction, approximately 55 bricks are used per square meter. This study examines four types of bricks: first-class, second-class, decorative (apparent or special), and spongy (refractory). Notably, the production of second-class bricks has been discontinued.

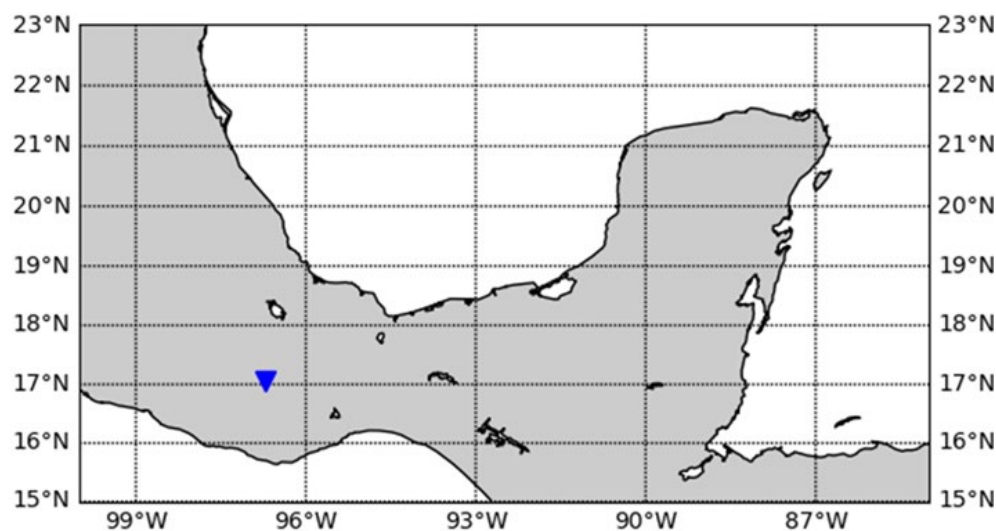


**Figure 1.** Geographical coordinates (blue triangle) for San Agustín Yatareni, Oaxaca, México.

The pores in fired red bricks typically include a range of types, from closed pores to interconnected voids, which influence their thermal insulation, mechanical strength, and moisture absorption properties.

### 3. Color Theory and Color Formats

The color wheel (see Figure 2a) is a graphical representation of colors, arranged in a circular spectrum and organized according to their relationships in terms of hue, saturation, and brightness [19,20]. In its most common form, the wheel includes primary colors (red, blue, and yellow), secondary colors (obtained by mixing two primary colors), and tertiary colors (created by mixing a primary color with a secondary color) (see Figure 2a). The color formats used in images are based on specific color models related to the color wheel. Understanding the relationship between the color wheel and color formats is essential for achieving effective and consistent visual results [21].

In Figure 3, the painting utilized to illustrate the methodology for estimating the moisture percentage is presented, while Figure 4 depicts the corresponding color formats derived from that painting.

The color values of a pixel in an image are typically represented using color models, such as the *RGB* (red, green, and blue) model or the *CMYK* (cyan, magenta, yellow, or black) model, depending on the device. Pixels are organized in rows and columns in a grid to form a complete image. The greater the number of pixels in an image, the higher its resolution, and, thus, its level of detail and visual quality. Image resolution is typically expressed in pixels per inch and determines the amount of detail that an image can present within a given physical space [21].

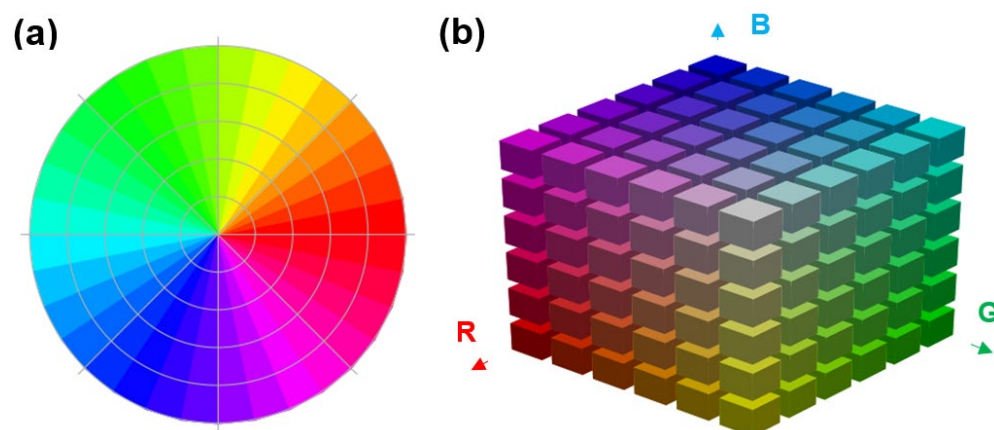


**Figure 2.** (a) Color wheel and (b) the RGB system.



**Figure 3.** Canvas image, *Sunset after the Rain*. Artist: Aida Andrea Pech Ricárdez, 2019.

Rooted in color theory and optics, the *RGB* (red, green, and blue) model is based on additive color synthesis, where different intensities of red, green, and blue light are combined to generate millions of colors [21]. In the *RGB* model, each color component is represented by a light intensity ranging from 0 to 255. By varying these intensities, colors can be mixed to produce everything from pure red to full-spectrum white light [21].

The *YUV* format is a critical standard in the video industry and in multimedia transmission, particularly for the representation and compression of images and video sequences. While less familiar than the *RGB* model, *YUV* is essential for encoding and transmitting visual content, especially in television and video applications. Originating in the color television industry, *YUV* is designed to align with human visual perception by focusing on the luminance (*Y*) and chrominance (*U* and *V*) components rather than on direct color representation, as in *RGB* [22]. The *YUV* model separates the brightness information (luminance) from the color information (chrominance), with luminance (*Y*) representing the image's brightness, and chrominance (*U* and *V*) capturing the color details. Specifically, the *U* component represents the difference between blue and luminance, while the *V* component represents the difference between red and luminance. This separation allows the *YUV* format to prioritize luminance, which significantly impacts the perceived image quality as changes in brightness are more detectable to the human eye than variations in color [22]. By focusing on luminance, the *YUV* format enables greater compression efficiency, reducing file sizes while maintaining visual quality. This is because the human eye is more sensitive to brightness differences than to color, allowing for a more aggressive compression of color information without noticeable degradation in image quality [22]. This efficiency is crucial for video transmission over networks and playback on mobile devices. Conversion

between *YUV* and *RGB* is necessary when displaying content on devices that use the *RGB* model, such as monitors and screens [22].

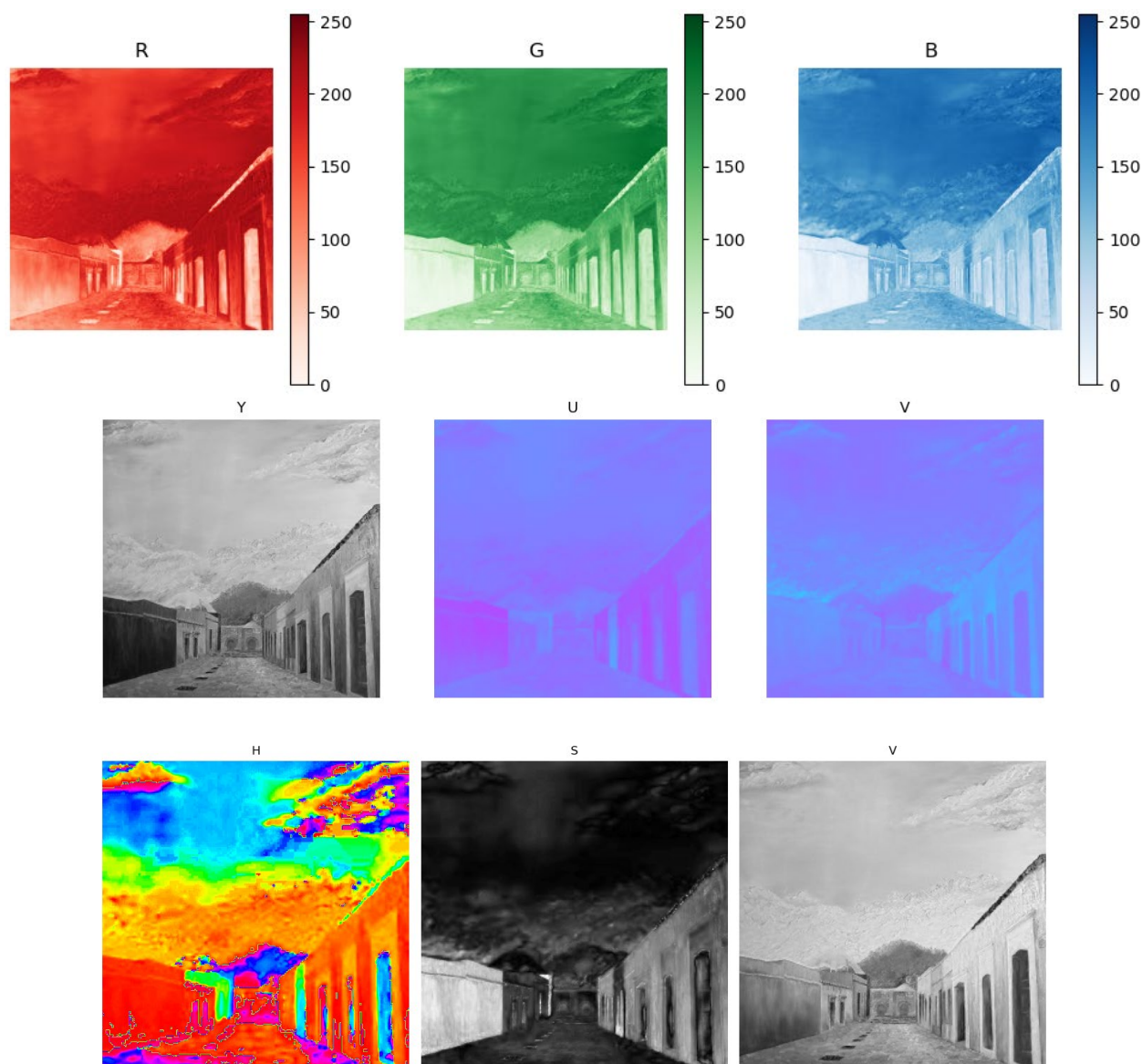


**Figure 4.** Color systems corresponding to the image illustrated in Figure 3. Systems: *RGB* (red, green, and blue), *YUV* (luminance, chrominance *U*, and chrominance *V*), and *HSV* (hue, saturation, and value).

The *HSV* (hue, saturation, and value) color model is a system that decomposes color information into three principal components: hue, which defines the color tone; saturation, which represents the intensity or purity of the color; and value, which determines the brightness or luminance of the color (see Figure 4) [22]. The *HSV* model is extensively utilized in image processing and computer graphics due to its ability to separate chromatic and luminance information. This separation facilitates the manipulation and detection of colors in applications such as image editing and computer vision. The *HSV* format allows for a more intuitive adjustment of colors and the detection of specific color ranges within an image. It is commonly used in tasks such as object segmentation, color adjustment during image editing, and edge detection [22].

#### 4. Artificial Intelligence: Unsupervised Learning

While color theory provides foundational insights into moisture-related color variations, artificial intelligence enhances our ability to quantify and interpret these changes across image datasets. AI algorithms can analyze historical data, climate patterns, budget constraints, and other factors to create optimal architectural designs. Notable examples include the work of the architect Michael Hansmeyer, who employs generative algorithms to create complex and visually stunning architectural structures. Recently, advanced programs for architectural design, such as MidJourney, have been developed [23]. The visual representations generated by these tools exhibit a high degree of aesthetic quality. AI demonstrates its precise processing capabilities by automatically incorporating the characteristics of an object into a digital image, even without explicit input in the form of keywords. Additionally, it is important to highlight the undeniable advantage of the speed at which these tools create outputs [24,25].

Unsupervised learning is a branch of artificial intelligence that focuses on processing data without labels or prior supervision. This technique is applied in four steps: in the first step, the attributes are extracted; in the second, dimensionality is reduced; in the third, data groups with similar characteristics are identified; and, in the fourth step, the segmented information is mapped back to the original image [18].

**(a) Attribute selection:** attribute selection in unsupervised learning involves choosing which features of the data are most important for the computer to correctly process the information. For example, if the goal is to identify the most illuminated regions of a painting, such as the one illustrated in Figure 3 [26], which depicts a perspective view of a tourist walkway in Oaxaca, attributes must first be extracted from a digital photograph of the painting. The computer must process the input information corresponding to these attributes to distinguish the regions of interest. Attributes can correspond to the various combinations of *RGB* or *YUV* values (see Figures 4–6) present in each pixel. In Figure 5, the attribute representing the contours of the buildings is visible. This attribute was obtained through a genuine combination of *RGB* values, wherein the edges were emphasized [27]. Identifying the most relevant attributes in an image may require several iterations to clearly determine which features are most significant [13,14]. Artistic paintings can display a diverse spectrum of tones, ranging from dark areas to bright and luminous regions. Similarly, images of construction materials, such as bricks, also reveal a distinct array of visual characteristics. In the *RGB* (red, green, and blue) color model, darker (“wet”) areas of a brick might be represented by lower values across each color channel, whereas brighter (“dry”) regions would be indicated by higher values. In contrast, when analyzing the same brick image within the *YUV* color space, the differentiation between dry and wet areas may be attributed to the luminance (*Y*) and chrominance (*U* and *V*) components. Here, luminance reflects the intensity of brightness, while chrominance captures subtle variations in moisture and texture. This comparison highlights how the choice of color representation can significantly influence the perception of visual characteristics, whether in artistic paintings or in construction materials. Once the key attributes are identified, the next step is to simplify data complexity through dimensionality reduction, ensuring that the essential visual characteristics are preserved for effective analysis.

**(b) Dimensionality reduction (PCA):** dimensionality reduction is an essential mathematical technique that simplifies multidimensional data, enabling more effective management of design projects. Figure 7 illustrates information related to three attributes derived from the painting presented in Figure 3. With these three attributes, the data can be visualized in three dimensions. Data can be projected onto a plane to facilitate simpler visualization. One of the most fundamental and powerful methods in this context is principal component analysis (PCA) [13,14]. PCA aims to transform a high-dimensional

dataset into a reduced set of variables, known as principal components. Figure 8 displays the results obtained after applying principal component analysis (PCA) to reduce the dimensionality of a problem associated with the study of attributes derived from the image of the painting shown in Figure 3. The objective is to automatically identify and isolate the most illuminated region of the painting. As mentioned before, in Figure 8, the dataset has been projected into a two-dimensional space, allowing for a clearer visualization of the different clusters associated with the various characteristics of the painting.

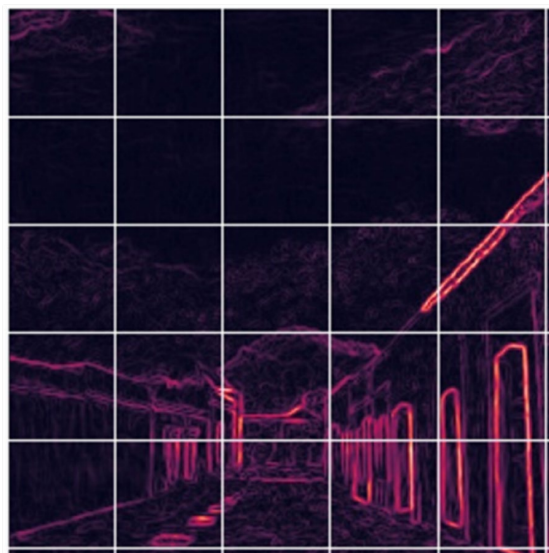


**Figure 5.** Attributes obtained by the application of the Sobel filter to the painting presented in Figure 3. This filter emphasizes the contours.

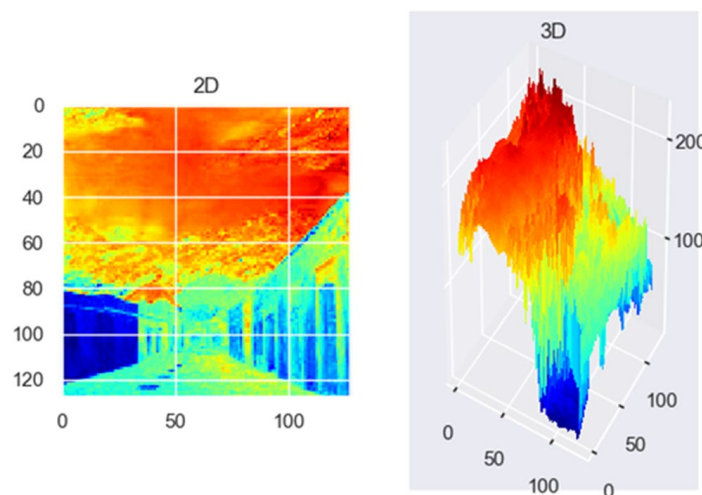


**Figure 6.** Images of the painting when considering the luminance in the *YUV* format. The red areas correspond to the brightest zones, while the blue areas indicate the darkest zones.

**(c) Clustering:** in the expansive realm of machine learning, clustering emerges as a powerful and versatile technique within the realm of unsupervised learning. Unsupervised learning is distinguished by its ability to extract knowledge from data without the use of prior labels, with clustering serving as a fundamental pillar in this domain [13,14]. Clustering, or group segmentation, is a process that involves dividing a dataset into groups or clusters, where the elements within each group are more similar to each other than to those elements outside the group. Figure 9 shows the result obtained after applying the K-means technique to detect three clusters of points.

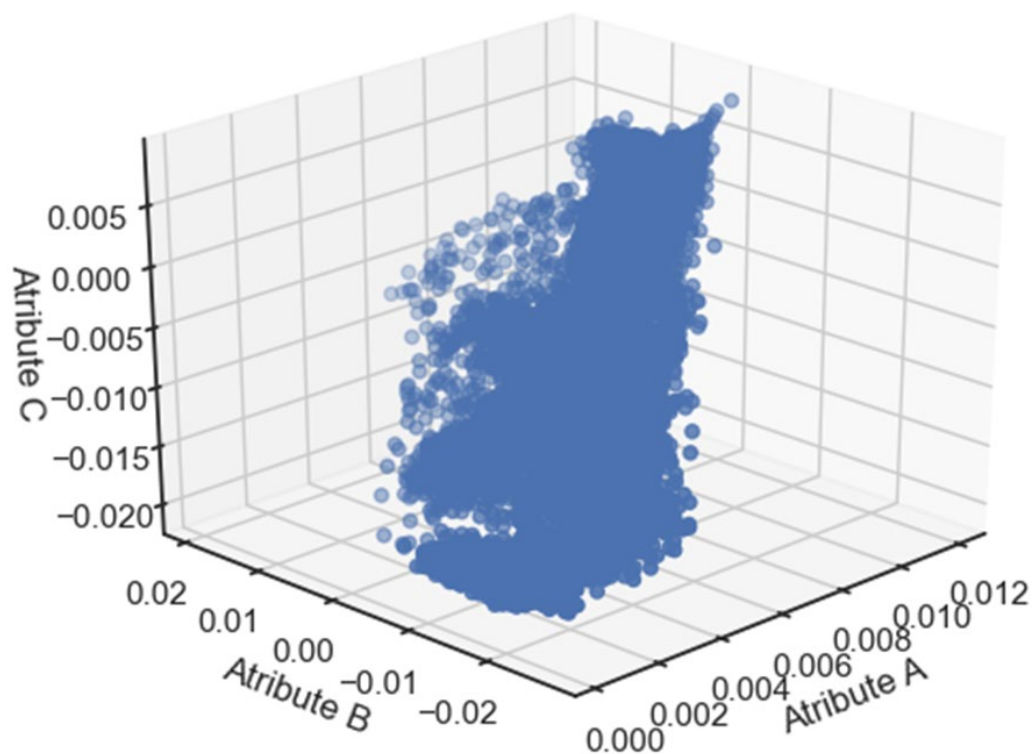


**Figure 7.** Graph illustrating the information corresponding to three attributes of the painting presented in Figure 3.

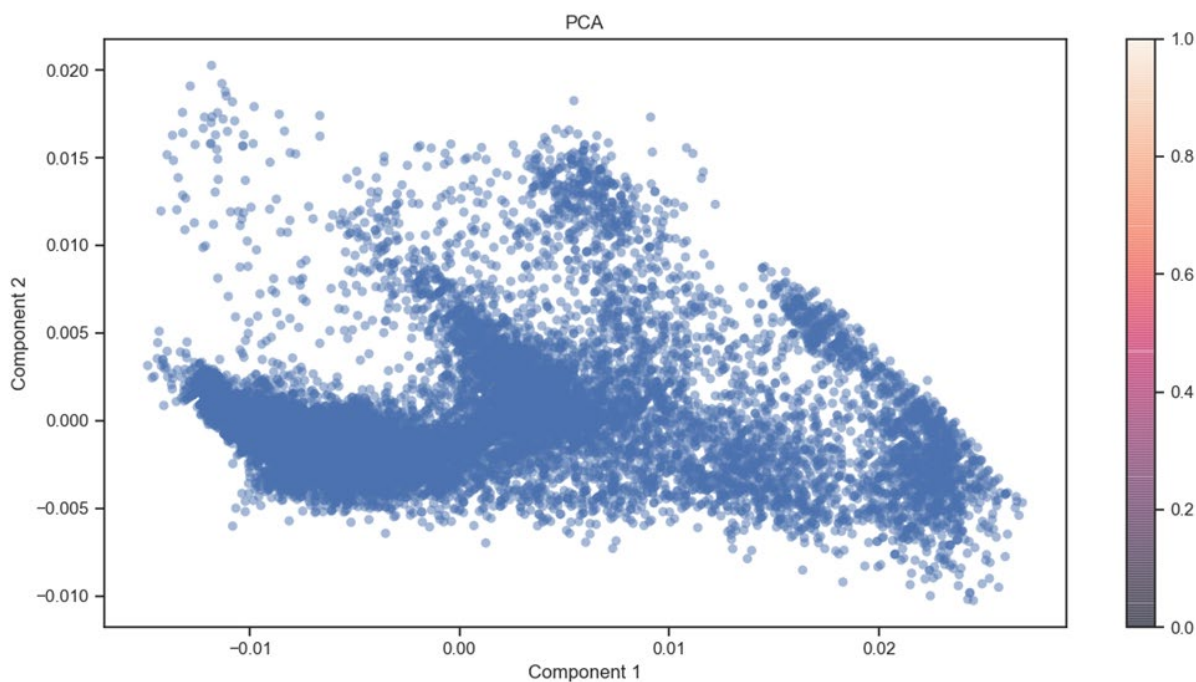


**Figure 8.** Application of the PCA algorithm to the attributes presented in Figure 7, which were obtained from the painting shown in Figure 3.

The clustering process is crucial for the organization, understanding, and simplification of complex data. Clustering has applications across a wide range of fields, making it an essential tool in data analysis [13,14].

For the painting previously described, the data clusters may be associated with combinations of various attributes derived from the *RGB* or *YUV* values. The number of attributes corresponds to the number of dimensions in the dataset.

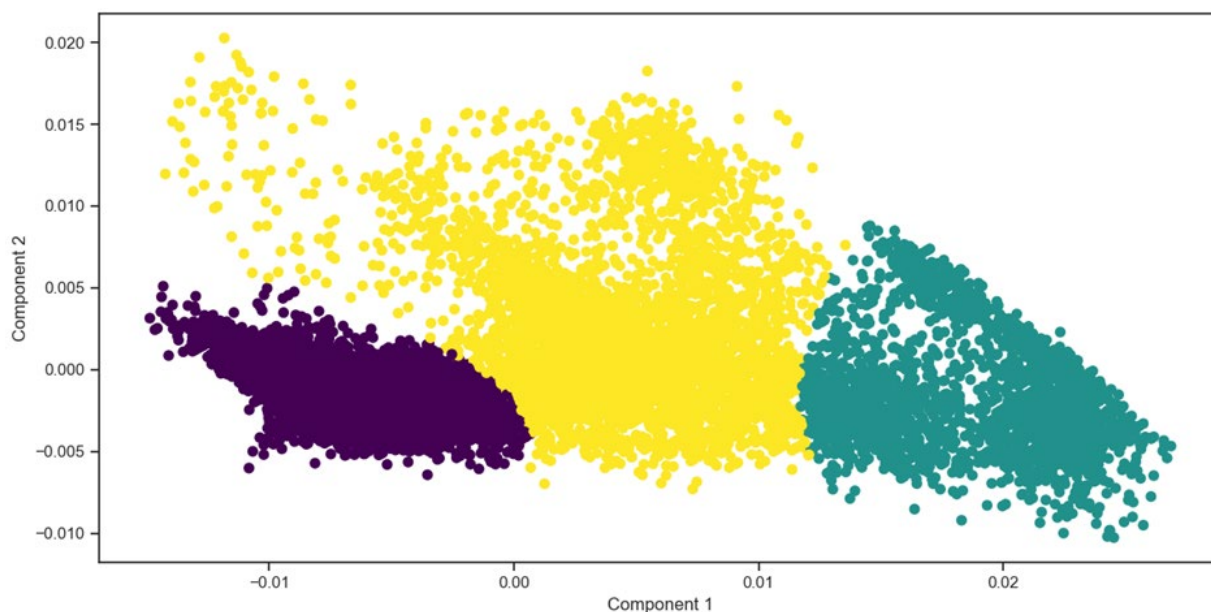


**Figure 9.** Application of the K-means algorithm to the attributes presented in Figure 7, which were obtained from the painting shown in Figure 3. The clusters identified by K-means are represented using different colors.

The K-means algorithm is used to identify and group similar data points into clusters. K-means groups the data points into clusters by repeatedly assigning them to the nearest centroid and updating the centroids until they stabilize.

The key advantage of the K-means algorithm is its simplicity and efficiency, making it fast and scalable for large datasets. It is easy to implement and understand, providing clear and well-defined clusters.

As mentioned before, Figure 9 illustrates the results obtained after applying the K-means technique to identify three clusters of points with similar characteristics.

The algorithm differentiates these clusters using distinct colors. Figures 10–12 present the various characteristics of the painting associated with the three groups identified through the application of PCA and the K-means algorithm.

Figure 12 shows a group of pixels corresponding to the most illuminated area of the painting, which was automatically identified by PCA and the K-means algorithm.

When applying principal component analysis (PCA) to paintings in *RGB* format, we analyze how the primary colors—red, green, and blue—combine to form the image. PCA identifies the color combinations that exhibit the greatest variability within the painting.

For instance, the analysis may reveal distinct combinations of blue and yellow in the depiction of a sky with clouds, while darker shades of blue and brown might be associated with areas representing buildings. In contrast, when PCA is applied to the *YUV* format, the analysis focuses on separating luminance (*Y*) from the chrominance (*U* and *V*) information.

Luminance corresponds to the brightness of the image, while chrominance conveys color and saturation details. PCA, when applied to the *YUV* format, may demonstrate that luminance is more critical for representing detail and intensity, whereas chrominance emphasizes color nuances and subtle variations. Similarly, when applying the K-means clustering to paintings in *RGB* format, we classify pixels based on their red, green, and blue values.

This method enables the identification of those regions within the painting that share similar colors. For example, the K-means algorithm might group the yellow pixels of the sky into one cluster and the blue pixels of the clouds into another. In the *YUV* format, the K-means algorithm would cluster pixels based on luminance and chrominance values,

facilitating the segmentation of the image into regions with similar brightness levels and color variations. In Figure 13, three groups are identified, which may correspond to the areas with buildings and the illuminated zone presented in Figure 3.

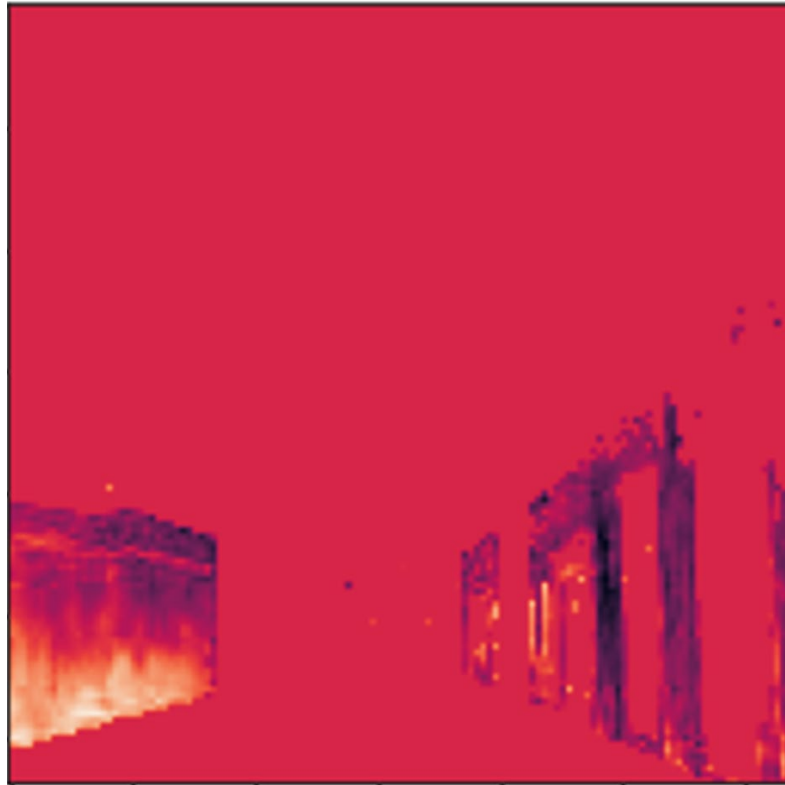


**Figure 10.** Cluster 1: a portion of the dark area of the painting illustrated in Figure 3.

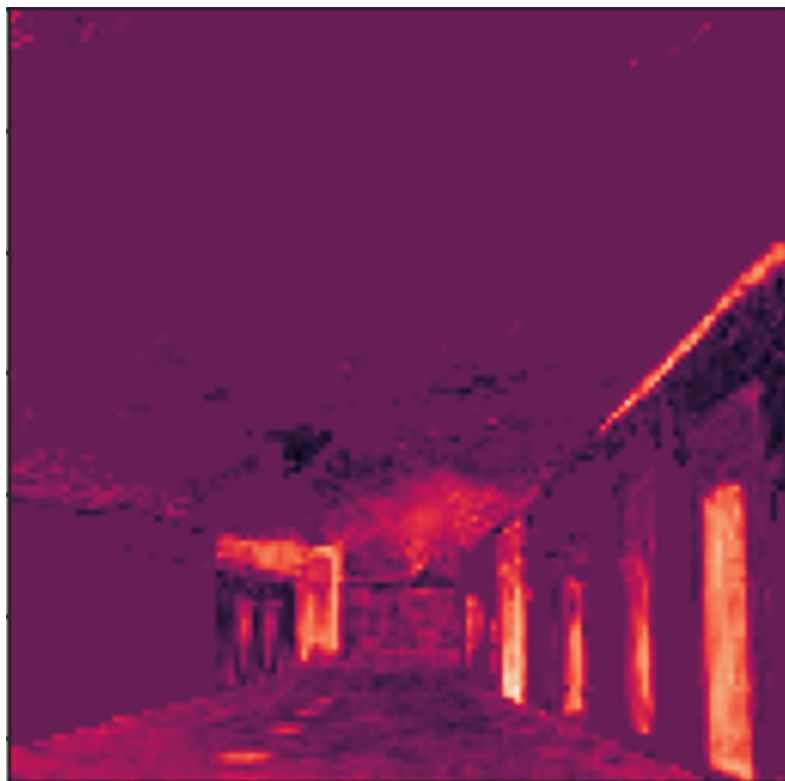


**Figure 11.** Cluster 2: a portion of the dark area of the painting illustrated in Figure 3.

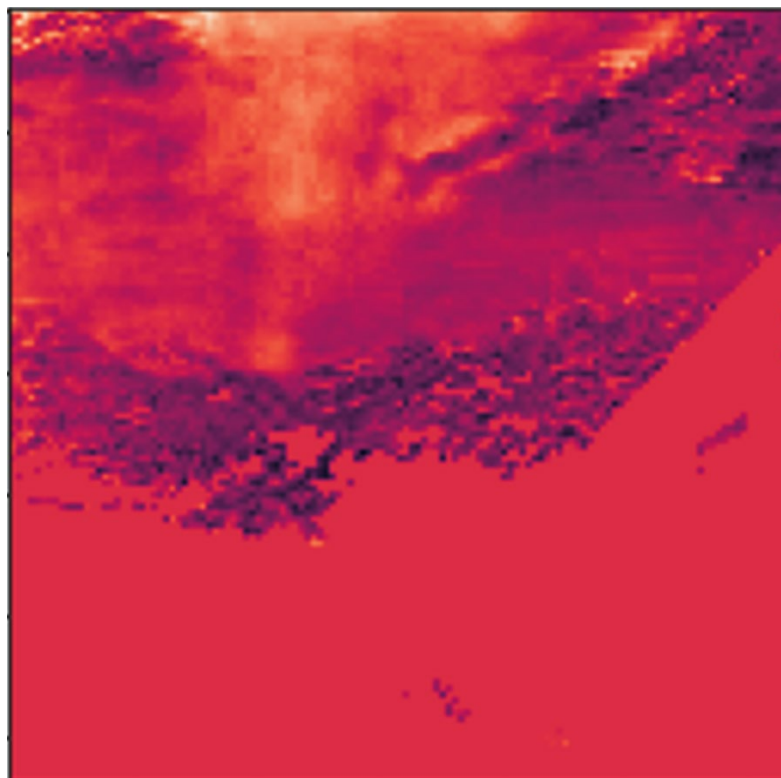


**Figure 12.** Cluster 3: the illuminated area (sky) of the painting illustrated in Figure 3.

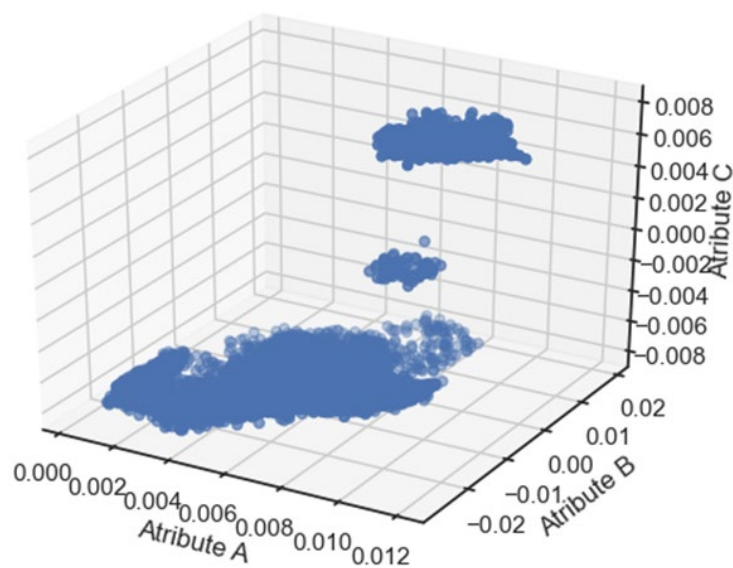


**Figure 13.** Graph illustrating the information corresponding to three attributes of the painting presented in Figure 3. One of the attributes was normalized.

PCA and K-means methods have their disadvantages. The primary limitations of PCA include its assumption of linear relationships and its extreme sensitivity to the scaling of attributes. Conversely, K-means clustering depends on the initial placement of centroids, is sensitive to outliers, and does not guarantee convergence [13,14]. PCA enables the visualization of data along the direction of maximum variance.

For instance, when taking a photograph of a group of people, the goal is to position them in such a way that everyone appears in the photo. If the people are arranged in a line, the direction of maximum variance aligns with the direction of the line [28].

Therefore, the camera should be positioned perpendicular to the line of people to capture everyone in the frame. PCA identifies new dimensions, known as principal components, which summarize the essential information of the dataset [13,14,28].

**(d) Image segmentation:** the illuminated region in Figure 12 was delineated through the application of K-means and PCA techniques. In this particular example, the clusters identified by the K-means algorithm exhibit some dispersion (see Figure 9).

This dispersion can be mitigated by combining and considering additional attributes. Figure 13 presents the clusters shown in Figure 7 in light of the modification of one of the attributes. Attributes are instrumental in data representation and in enhancing the algorithm's ability to uncover patterns and hidden structures. Certain attributes may be more informative for a specific problem. Informative attributes significantly influence clustering and dimensionality reduction as they contain critical information about the underlying data structure.

Some unsupervised learning algorithms are capable of capturing nonlinear relationships or interactions between attributes, while others may be less sensitive to these factors. As described above, in Figure 13, three distinct groups are observed, which may correspond to those areas with buildings and the illuminated zone of the painting (Figure 3).

It is essential to emphasize that PCA identifies the directions of maximum variance in the data, often revealing underlying trends and relationships between the variables. This helps to reduce data complexity while preserving essential information.

In contrast, the K-means algorithm clusters data based on similarities, facilitating the identification of natural groupings within the data. By combining PCA and K-means methods, it is possible to detect complex patterns that might not be immediately apparent, aiding in informed decision-making and the extraction of valuable insights from complex datasets. Figure 14 shows the result of applying PCA to the data presented in Figure 13.

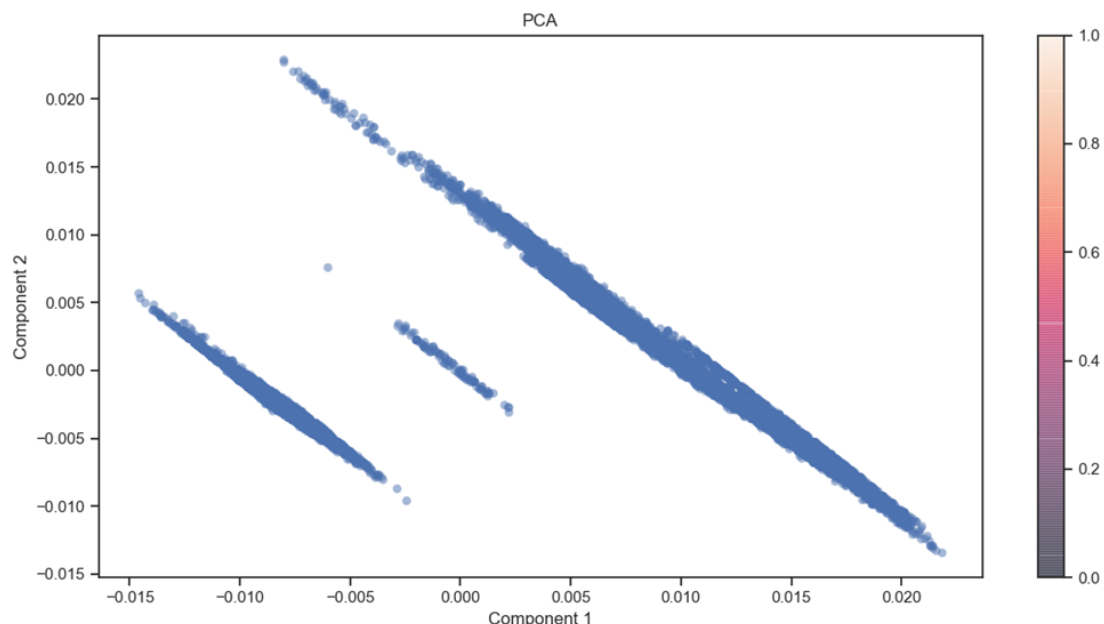


**Figure 14.** Application of PCA to the attributes illustrated in Figure 13.

In contrast, Figure 15 presents the outcome of applying K-means clustering to the data shown in Figure 14. In PCA, appropriate attribute selection enhances the capture of principal variations, while irrelevant attributes will negatively impact simplification.

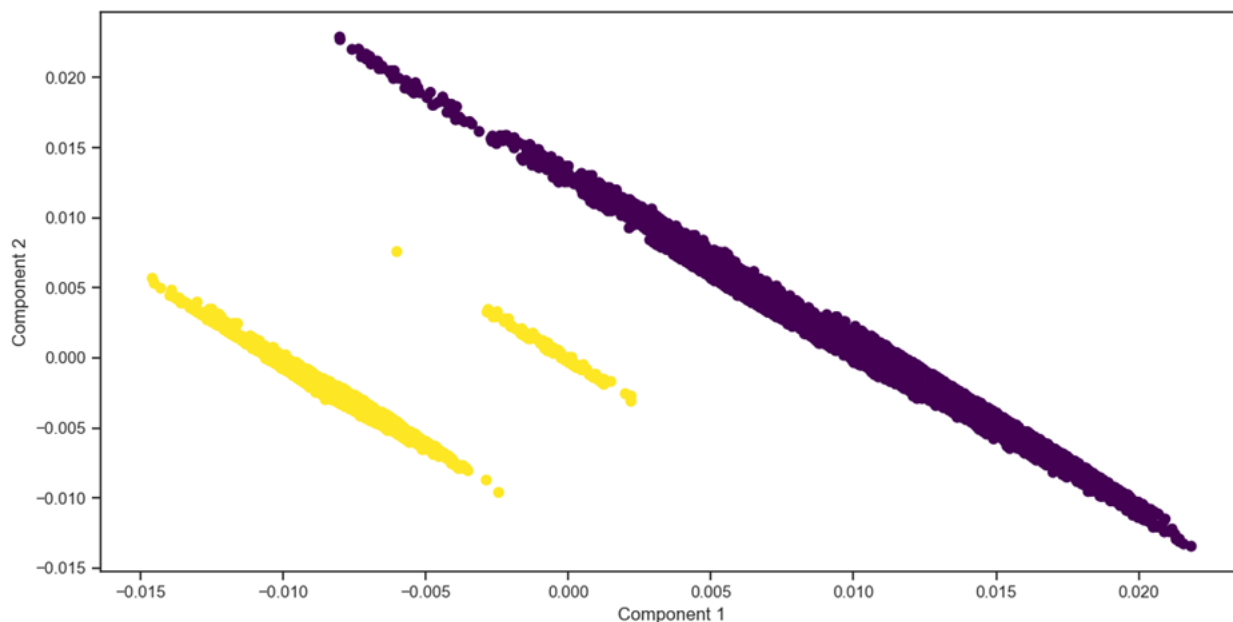


**Figure 15.** Application of the K-means algorithm to the points shown in Figure 14.

In K-means analysis, the choice of attributes affects the quality of the clusters, potentially leading to erroneous groupings [13,14].

Figures 16 and 17 present the images associated with those regions that correspond to the sky and buildings of the painting shown in Figure 3. Similar to its application in painting restoration, PCA could be employed to highlight the most relevant features that influence the estimation of moisture levels in bricks.



**Figure 16.** Cluster 1: the dark area of the painting illustrated in Figure 3, considering the attributes illustrated in Figure 13.

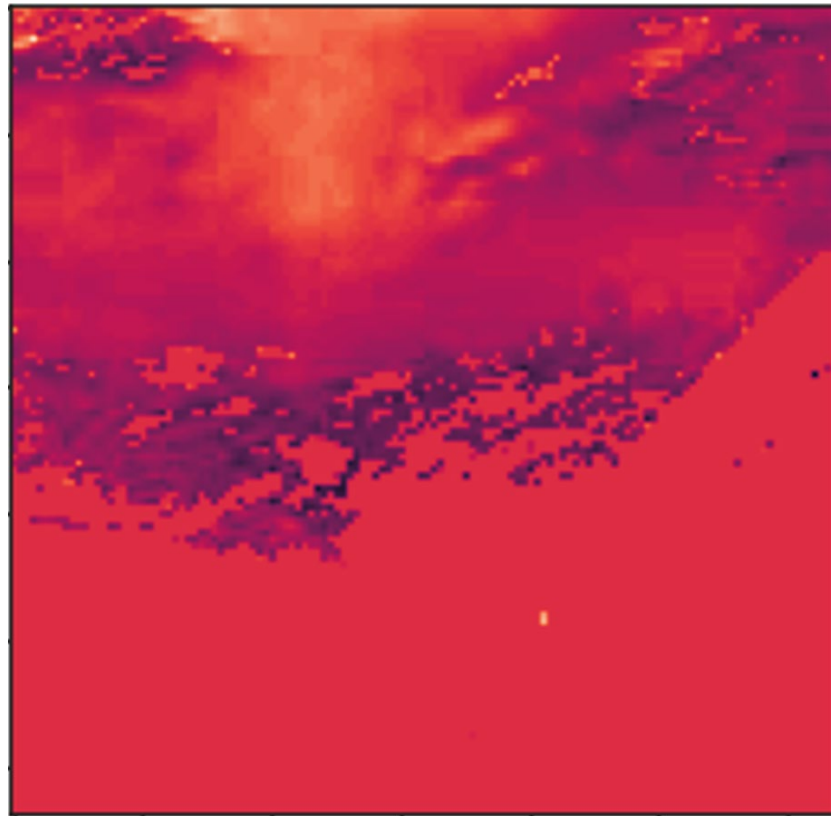


**Figure 17.** Cluster 2: the illuminated area of the painting illustrated in Figure 3, considering the attributes illustrated in Figure 13.

Applying PCA to artworks, such as paintings, helps identify significant details like colors or patterns; its application to brick images can reveal textural patterns, color variations, and visual features related to moisture.

## 5. Mexican Norms Utilized in This Study

- (a) NOM-018-ENER-2011 [29]: “Thermal Insulators for Buildings. Characteristics and Testing Methods”
  - Objective: to establish the technical requirements for thermal insulators to ensure effective heat transfer control in construction.
- (b) NMX-C-228-ONNCCE-2010 [30]: “Construction Industry. Thermal Insulating Materials. Determination of Moisture Adsorption and Water Absorption”
  - Objective: to standardize the method for assessing moisture adsorption and water absorption in thermal insulating materials.
- (c) NMX-C-037-ONNCCE-2013 [31]: “Construction Industry. Masonry. Determination of Total and Initial Water Absorption in Blocks, Bricks, or Masonry Units. Testing Method”
  - Objective: to provide a standardized test for measuring water absorption in masonry materials.
- (d) The NMX-C-404-ONNCCE-2012 [32] standard specifies the requirements and testing methods for the ceramic bricks used in construction. This standard guarantees the quality and durability of ceramic bricks in buildings.

## 6. Methodology

Images of the four types of bricks showing varying moisture levels were obtained. Images corresponding to the fired red bricks, categorized as first-class, second-class, ap-

parent, and spongy, were obtained. These bricks are predominantly used in residential construction in the state of Oaxaca. For all images, the smartphone was positioned at the same distance from the brick under consistent illumination conditions. One face of the brick, associated with its largest dimension, was in contact with the free water surface to ensure the capillary rise of the water. First-class bricks are characterized by their red color, which is derived from the clay used and the high temperatures applied during the firing process. Their rough texture and rustic appearance also contribute to their aesthetic appeal. In construction, first-class fired red bricks are highly regarded, not only for their traditional look but also for their structural load-bearing capacity, making them a versatile and reliable material.

The second-class fired red brick, depicted in Figure 18a, differs from the first-class brick in that it often exhibits imperfections or aesthetic defects, such as color variations, deformations, or irregular dimensions. These characteristics make it less suitable for applications that require a uniform and attractive appearance. However, the second-class brick is a more economical alternative to the first-class brick, making it appropriate for projects where aesthetics are not the primary concern and budget constraints are significant. It is essential to ensure that this brick meets the standards set by relevant building codes, particularly in regions like Oaxaca, which is located in a highly active seismic zone.



**Figure 18.** Images of: (a) second-class brick, (b) spongy brick, (c) first-class brick, and (d) apparent brick, showing the presence of moisture. In the experiments, water rises by capillarity. The experiment involved placing the base of the brick in direct contact with water, enabling the upward movement of water through capillary action. To systematically assess this process, the height of the brick was divided into increments of one centimeter. At each defined height, a photograph was captured using a smartphone to document the progression of the water front visually. Additionally, the weight of the brick was recorded under two conditions: first, when the brick was completely dry, and subsequently, as the water invasion front reached each incremental height.

The apparent fired red brick is a prominent construction material renowned for its traditional aesthetics and durability. Characterized by its red hue, which is derived from the clay and high-temperature firing process, this brick features a rough, textured surface that adds rustic charm. The surface of the apparent brick is rich in minerals, including quartz. Due to its versatility, the apparent fired red brick is employed in various applications, including exterior cladding, walls, and fireplaces, offering both aesthetic appeal and functional benefits in architectural projects.

Figure 18b shows the presence of variable moisture due to capillary water rising in the fired red brick type known as spongy. The permeability of this brick can vary in different areas due to reasons related to its manufacturing and composition, which are described below.

- Variability in firing: the temperature and firing time may not be uniform. This can result in certain areas of the brick being more fully fired. Extremely well-fired areas may become less permeable.
- Variations in composition: the exact composition of the clay or the material used to make bricks can vary in different parts of the raw material.
- Density and compaction: during the manufacturing of bricks, the material is compacted into molds before firing. The way in which the material is compacted can vary, affecting the density and porosity of the brick in different areas. Less well-compacted areas may be more permeable than more well-compacted areas.

Table 1 presents the moisture percentage values for the different types of bricks. Figures 19 and 20 present images of the spongy, apparent, first-class, and second-class bricks using different color formats such as RGB, YUV, and HSV.

**Table 1.** Moisture percentages for the different types of bricks.

FIRST CLASS	Kg	Time	%H
0 cm	2.740	11:13	
3 cm	2.840	11:24	3.52
4 cm	2.870	11:32	4.52
5 cm	2.920	11:48	6.16
6 cm	2.955	12:01	7.27
7 cm	2.985	12:19	8.2
8 cm	3.015	12:26	9.12
9 cm	3.045	12:39	10.01
10 cm	3.075	12:54	10.89
APPARENT	Kg	Time	%H
0 cm	2.275	12:57	
3 cm	2.345	1:01	2.98
4 cm	2.360	1:03	3.60
5 cm	2.375	1:06	4.21
6 cm	2.385	1:08	4.61
7 cm	2.405	1:12	5.40
8 cm	2.420	1:17	6.00
9 cm	2.440	1:23	6.76
10 cm	2.460	1:29	7.52
SPONGY	Kg	Time	%H
0 cm	2.470	1:31	
3 cm	2.510	1:34	1.59
4 cm	2.525	1:36	2.17
5 cm	2.540	1:39	2.75
6 cm	2.550	1:43	3.13
7 cm	2.560	1:46	3.51
8 cm	2.575	1:52	4.07
9 cm	2.585	1:56	4.44
10 cm	2.6	2:07	5
SECOND CLASS	Kg	Time	%H
0 cm	2.445	6:29	
3 cm	2.525	6:36	3.16
4 cm	2.560	6:43	4.49
5 cm	2.595	6:51	5.78
6 cm	2.620	6:58	6.67
7 cm	2.660	7:11	8.08
8 cm	2.685	7:20	8.93
9 cm	2.715	7:29	9.94
10 cm	2.750	7:42	11.09

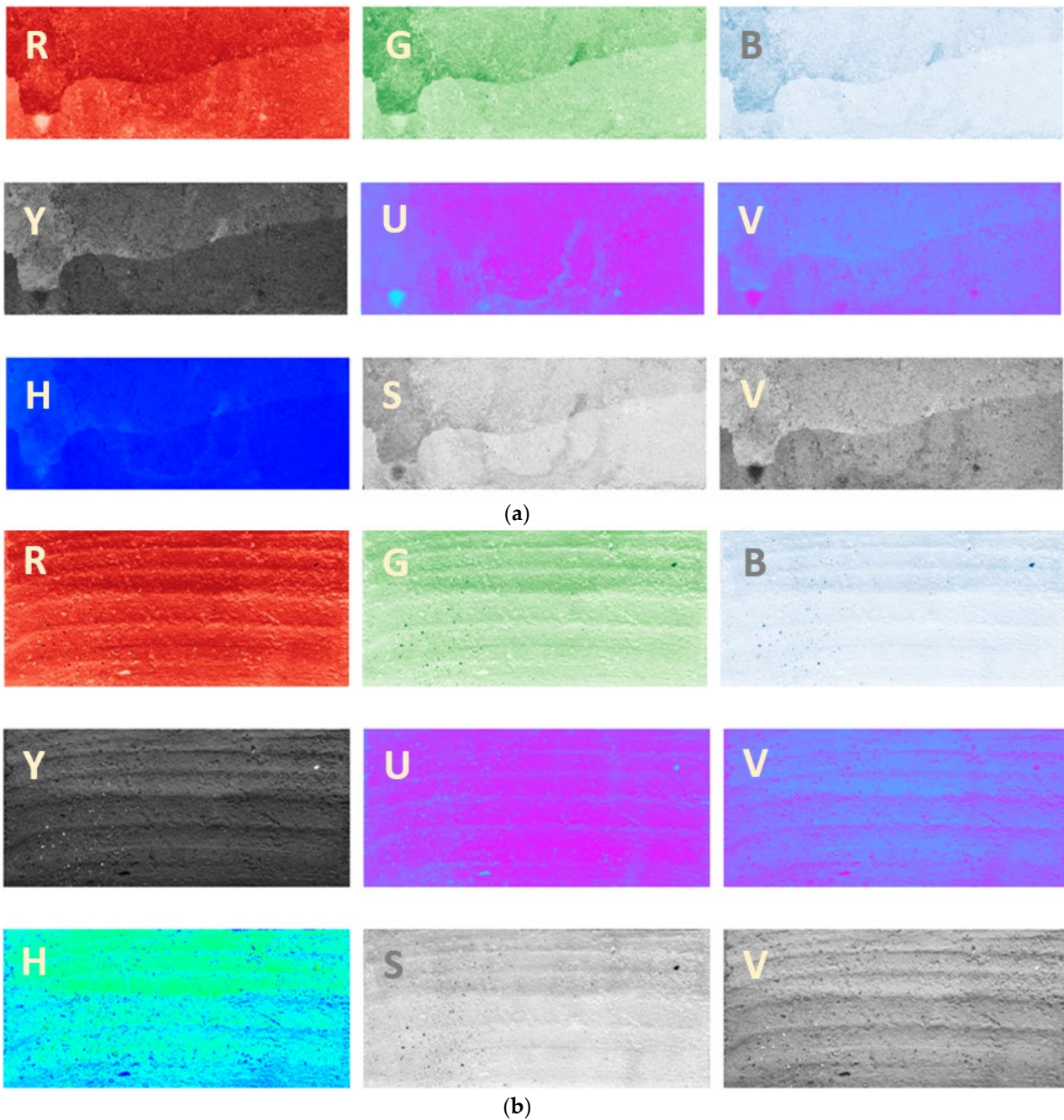


**Figure 19.** RGB, YUV, and HSV image formats of: (a) spongy and (b) apparent bricks.

The images, in RGB, YUV, and HSV formats, obtained from fired red bricks can provide indirect information regarding moisture, as follows:

- RGB (red, green, and blue). Changes in color intensity, especially in darker tones, can indicate areas of the brick surface affected by moisture. Wet areas tend to show darker colors or color variations, which may be an indication of moisture problems.
- YUV. The luminance (Y) in the YUV color space can be useful for detecting differences in surface reflectance. Wet areas tend to reflect less light, which could manifest as lower luminance in the image.
- HSV (hue, saturation, and value). Saturation and value in the HSV color space can help identify areas with different water contents. Wet areas may show different saturation levels and values compared to dry areas.

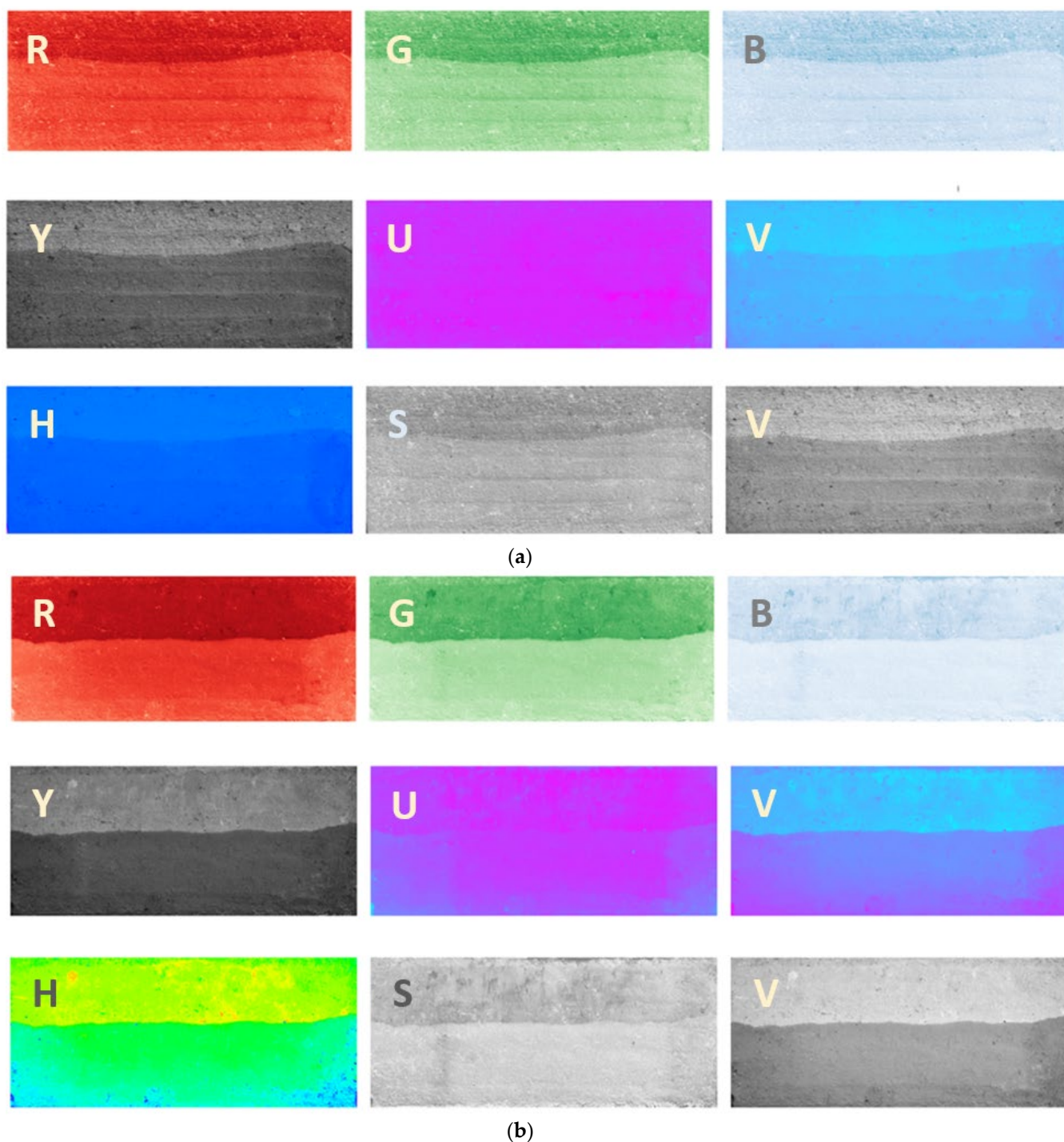


**Figure 20.** RGB, YUV, and HSV image formats of: (a) first-class and (b) second-class bricks.

This is important when building inspection and quality control applications to detect moisture problems that can affect the structural integrity and energy efficiency of a building [6]. In-depth moisture analysis typically requires specific sensors and measurement techniques. However, images in the aforementioned formats can provide an initial visual indication of moisture problems.

Analyzing images in various formats enables the assessment of texture and coloration differences in bricks, which may correlate with their permeability and overall quality. This approach can assist in material inspection and construction quality control. Additionally, image analysis facilitates the inference of mineral presence and distribution within fired bricks, contributing to their mineralogical characterization. However, precise mineral

identification often requires advanced techniques such as microscopy and X-ray diffraction. While color images provide an initial overview of mineral composition, they cannot replace these detailed analytical methods. However, the surface texture characterization of bricks can be enhanced through image analysis. The *HSI* (hue, saturation, and intensity) format, employed in video technology and adapted by previous researchers to study fluid content [33], is illustrated in Figure 21, demonstrating its application.

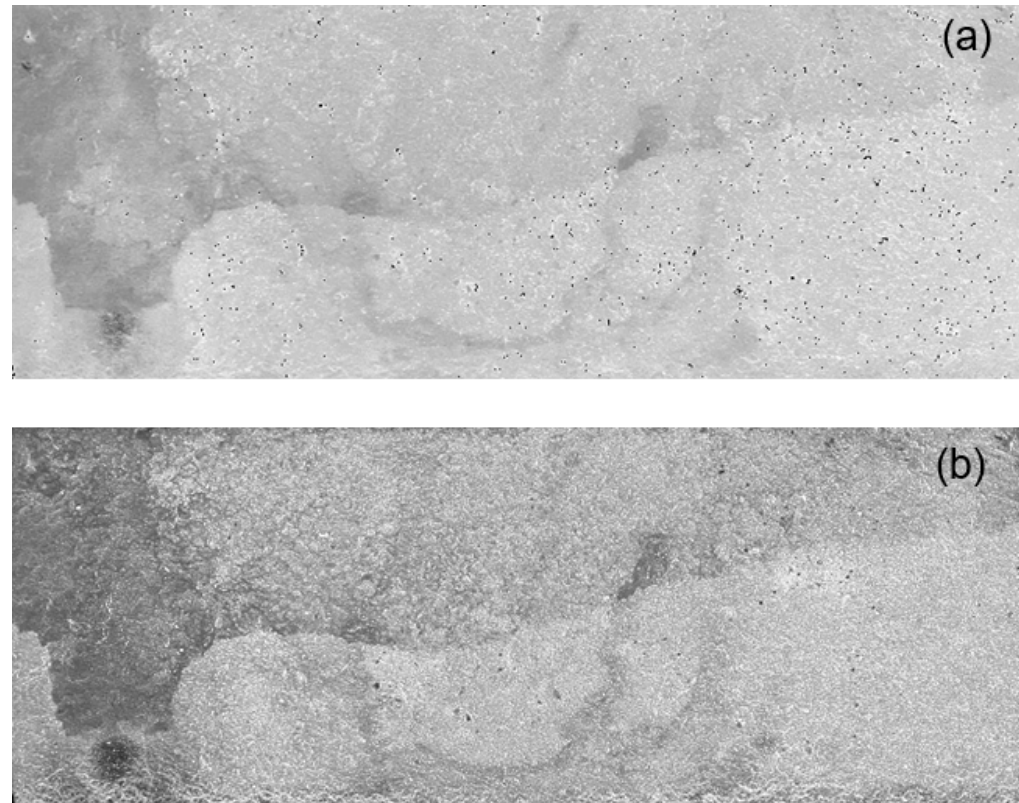


**Figure 21.** (a) Hue and (b) saturation of the spongy brick corresponding to the *HSI* format, which is similar to the Munsell format used in geology. Hue and saturation seem to correlate with moisture and texture, respectively.

Attributes, derived from photographs, encompass specific measures such as *RGB* or *YUV* amplitudes. Analogous to the *RGB* color model in image representation, which decomposes an image into three color components, seismic attributes in geophysics disaggregate the seismic data into features like amplitude, frequency, and wave velocity. This process provides a detailed view of subsurface conditions, similar to the way in which the *RGB* model enables a broad range of color representation in images. Seismic attributes thus facilitate a comprehensive characterization of geological and structural properties, enhancing geophysical exploration and assessment [18].

Digital image processing, augmented by artificial intelligence, enables the analysis of fired red brick images to estimate moisture content effectively. Through unsupervised learning, AI can detect key characteristics related to moisture—such as texture, color, and the distribution of moisture spots—directly from photographs. This advanced methodology streamlines the evaluation process and improves accuracy in moisture percentage estimation, offering significant benefits for research and practical applications in the construction industry and building conservation. Figure 22 illustrates the application of principal component analysis (PCA) to specific attribute combinations, as shown in Figure 20, for the second-class brick.

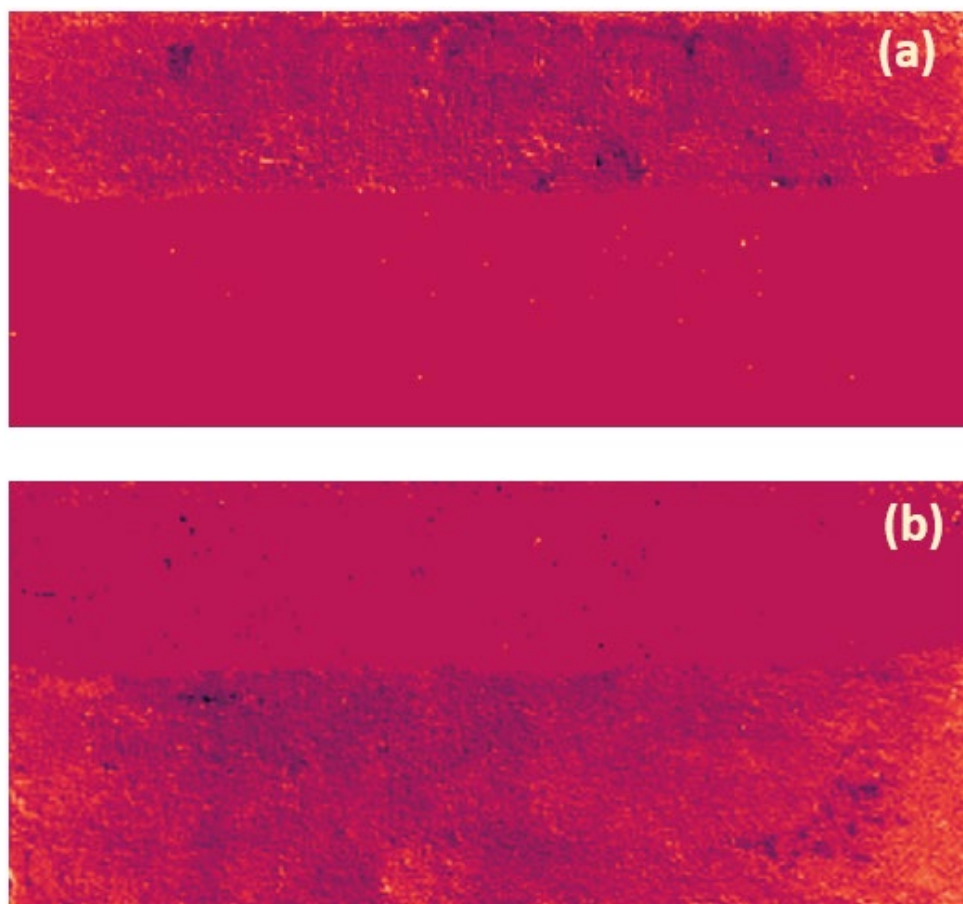


**Figure 22.** Segmented images corresponding to the second-class brick illustrated in Figure 18a: (a) dry and (b) wet areas.

With color intensity variations providing initial moisture indicators, further insights are obtained through clustering techniques that categorize the image data into distinct moisture-related patterns. As mentioned before, the K-means algorithm is a robust clustering technique that is widely used in data mining and machine learning. It partitions a dataset into clusters in which the points within each cluster exhibit high similarity. The algorithm iteratively assigns data points to these clusters and updates the cluster centroids. Its simplicity and efficiency are valuable for pattern recognition in unlabeled data, though its performance can be influenced by the initial centroid selection and the number of clusters. K-means clustering identifies the moisture levels in images, distinguishing between the dry and wet areas of a brick wall. Analyzing these clusters reveals the moisture distribution patterns, offering insights into how moisture varies and its correlation with material characteristics. Comparison of segmented images (Figure 22a,b) with the reference photograph (Figure 18a) indicates that the unsupervised learning approach used in digital image processing is robust and reliable. These clusters not only reveal moisture distribution but also set the stage for estimating moisture levels by calculating relative amplitudes from the segmented images. For more detailed moisture analysis, additional clusters are recommended.

#### 6.1. Estimation of Moisture Percentage and Hydraulic Diffusivity

First, the volume of water added to the brick via capillarity is calculated using the following formula:

$$\%H = \left( \frac{P_Z - P_S}{P_Z} \right) 100 \quad (1)$$

considering the different heights (3, 4, 5, 6, 7, 8, 9, and 10 cm) of the invasion front in the brick.  $P_Z$  corresponds to the weight of the wet brick (considering that the height of the invasion front is  $Z$ ) and  $P_S$  corresponds to the weight of the dry brick. For each value of  $Z$ , a corresponding table is generated, where multiple specimens are analyzed. Subsequently, the light intensities for both the wet and dry regions, denoted as  $I_H$  and  $I_S$ , respectively, are calculated for each height.

The light intensity is calculated as  $I = (R + G + B)/3$ , where  $R$ ,  $G$ , and  $B$  correspond to the values of the red, green, and blue channels of the  $RGB$  format. Figure 23 shows a typical image of the  $G$ -channel and its respective amplitudes, which correspond to the second-class brick. To achieve more accurate estimates of light intensities and reduce errors, the average  $RGB$  values were obtained from the central areas of both the dry and wet regions (see Figure 24). Using the values  $I_H$  and  $I_S$  for each height, the luminosity percentages were calculated using the following expression:

$$\%L = \left( \frac{I_S - I_H}{I_H} \right) 100 \tag{2}$$

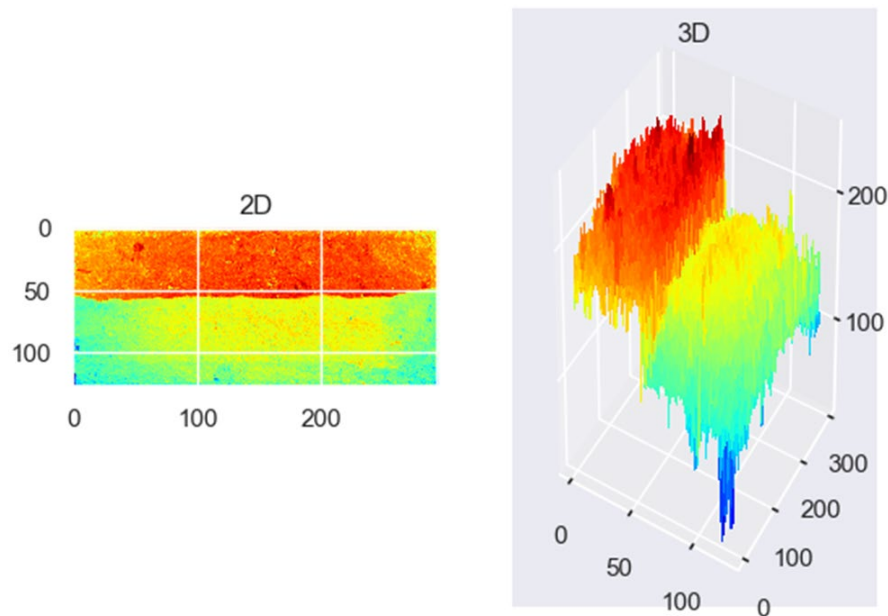


Figure 23. The  $G$  layer of the image shown in Figure 18a.

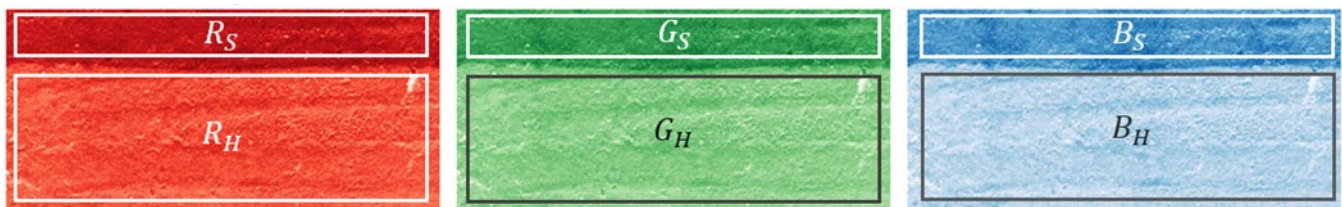


Figure 24. Typical regions for which the average values of the  $RGB$  layers were calculated.

Using this approach, luminosity percentages were calculated for varying heights of the invasion front. The moisture percentage in a brick sample can then be correlated with the relative difference between the average light intensity values in the dry and wet regions of the image, as follows:

$$L = f(H) \tag{3}$$

where  $f$  is an expression that correlates the moisture percentage with the luminosity percentage, as defined by Equations (1) and (2). Moisture percentages in the brick sample

and luminosity values in the image were estimated to subsequently adjust the coefficients in Equation (3). The selection of these coefficients is contingent upon the specific experimental conditions and on the relationship between luminosity percentage and water content in the samples. The relative difference in luminosity values, which represent the average of the color layer values between the dry and wet areas in an image, can mitigate the influence of lighting variations. This relative difference serves as a form of internal normalization, accounting for lighting variations that affect both areas equally. However, several additional considerations must be addressed:

- Uniformity of lighting: significant lighting disparities within the image may limit the effectiveness of this procedure.
- Additional corrections: in cases where lighting is a critical factor, additional corrections to the images may be necessary to ensure reliable estimates.

It is worth emphasizing that using the relative difference in luminosity between dry and wet areas can be an effective strategy to mitigate the impact of lighting on measurements. However, the effectiveness of this technique is contingent upon the uniformity and variability of lighting conditions. Therefore, careful analysis and additional corrections are always advisable. The relationship between moisture content and the relative difference in average luminosity values can provide significant insights and facilitate the detection of water content in porous materials. Potential interpretations of this relationship include:

- Water content indicator: the relative difference in luminosity values between dry and wet areas may serve as an indicator of the presence of water in the brick sample.
- Sensitivity to capillarity: this analysis technique may be sensitive to capillarity effects, as changes in water content can impact luminosity values.
- Non-destructive monitoring: this relationship can be useful for the non-destructive monitoring of water content in bricks or similar materials.
- Process control: in industrial applications, this relationship could be used as a process control tool to monitor and ensure appropriate moisture levels during brick production or other porous material manufacturing.

The construction of the expression that relates moisture and luminosity percentages is described below. Figures illustrating this information display the results from various examples. As previously mentioned, Figure 24 shows the areas used to estimate luminosity intensities in the dry and wet zones. The luminosity intensities represent the averages of the  $R$ ,  $G$ , and  $B$  values in each of the studied regions, which are then used to calculate luminosity (as shown in Equation (2)).

The luminosity percentage, as defined by Equation (2), was estimated for various invasion front heights. It is important to note that variations in pixel size can influence these percentages due to the fractal nature of the experiment, as observed in previous studies on rock porosity [34]. Fractals, characterized by repeating patterns at different scales, have a mathematical connection to nature [35].

Figures 25 and 26 illustrate the variations in the moisture percentage of the bricks, relative to the square root of the invasion time, and the height of the invasion front ( $Z$ ), respectively. Figure 27 displays a graph of the luminosity and moisture percentages for different bricks, with a consistent pixel size being used in all cases. Figure 28 shows the hue and moisture percentages for different bricks, with a consistent pixel size being used in all cases.

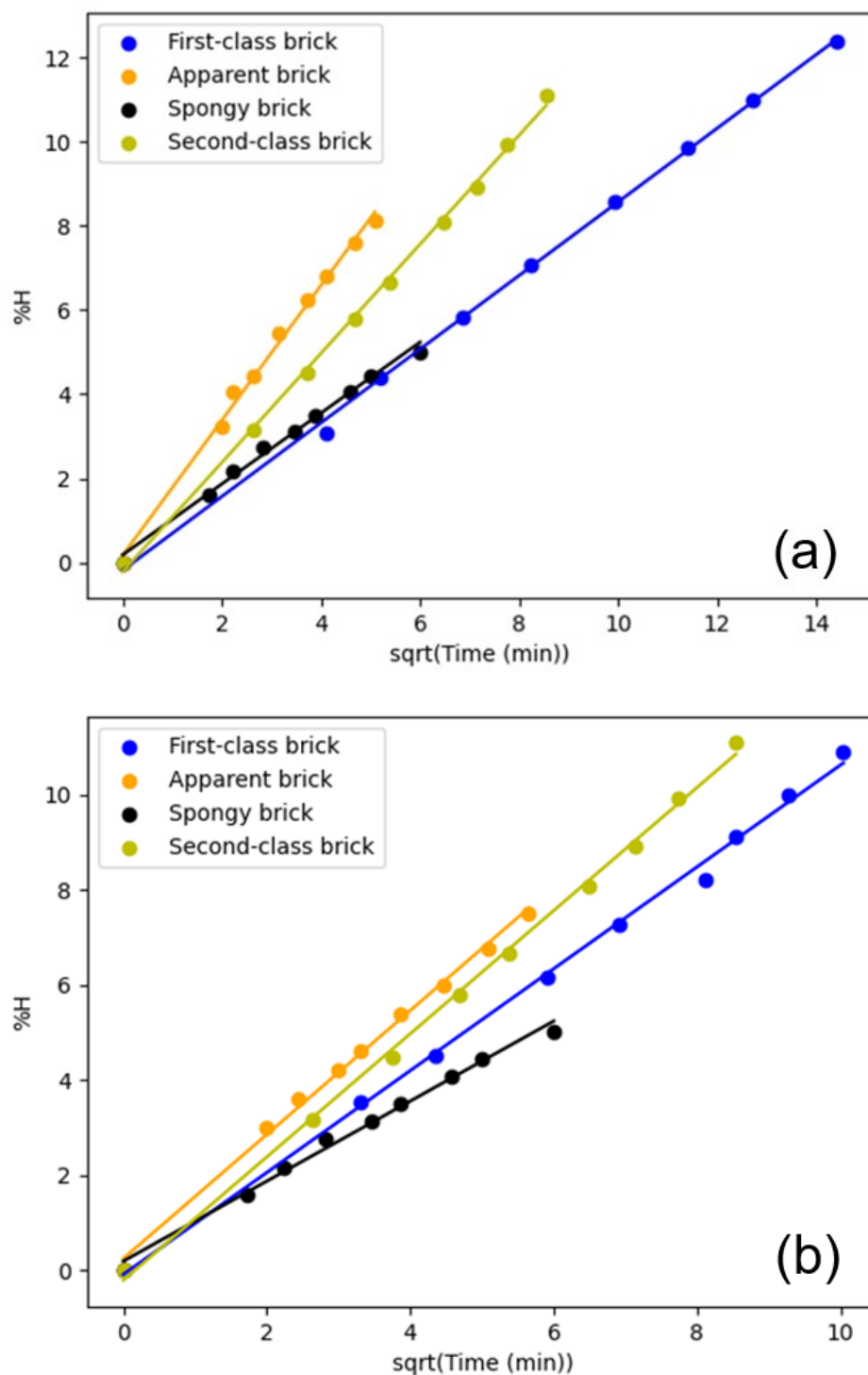


**Figure 25.** The vertical and horizontal axes represent the percentage of moisture and the square root of time, respectively. (a) The coefficients of the lines and residuals (the sum of the squares of the fit errors) are: [0.8751 -0.1799], 0.1664; [1.6018 0.1751], 0.2440; [0.8420 0.1843], 0.1491; [1.2959 -0.2143], 0.1771. (b) The coefficients of the lines and residuals (the sum of the squares of the fit errors) are: [1.0720 -0.0943], 0.2750; [1.3047 0.2398], 0.1520; [0.8420 0.1843], 0.1491; [1.2959 -0.2143], 0.1771.

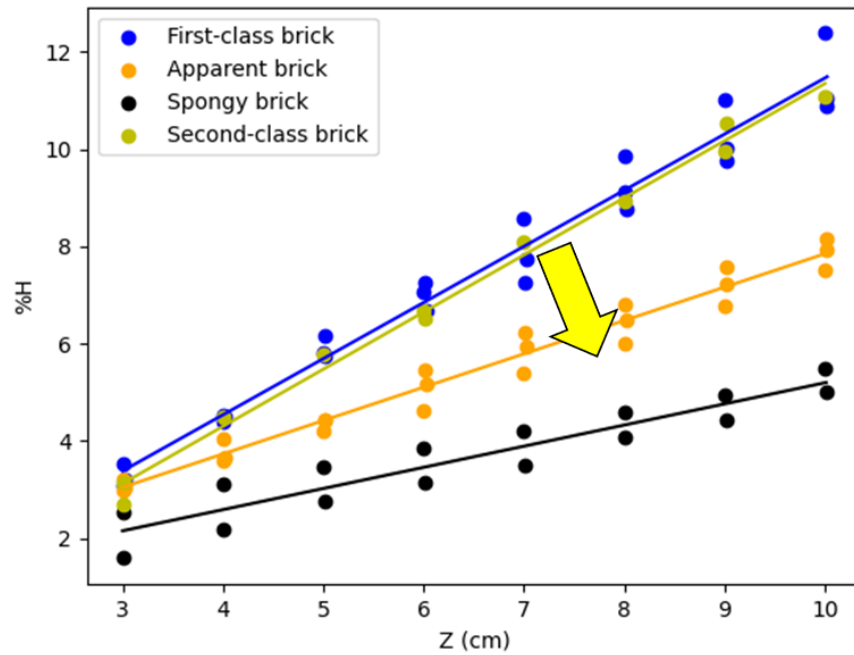


**Figure 26.** The vertical and horizontal axes represent the percentage of moisture (Equation (1)) and the height of the front of invasion, respectively. The arrow indicates the direction in which the permeability and the size of the voids increase. The coefficients of the lines and residuals (the sum of the squares of the fit errors) are: [1.1542 -0.0812], 4.5464; [0.6860 0.9874], 1.7723; [0.4348 0.8469], 2.0793; [1.1747 -0.4008], 0.6729.

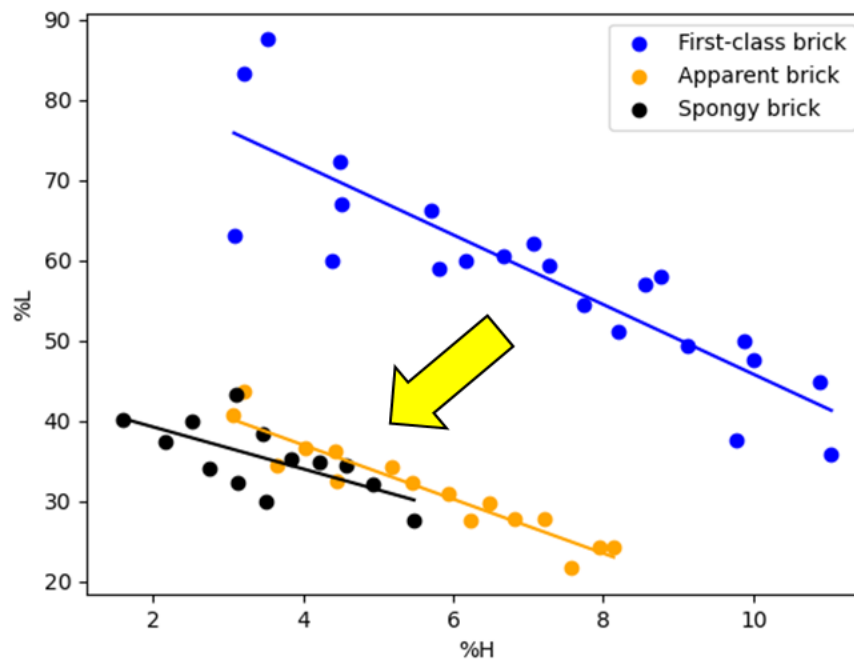


**Figure 27.** Graph illustrating the function defined by Equation (3) for different types of bricks. The arrow indicates the direction in which the permeability and the size of the voids increase. The coefficients of the lines and residuals (the sum of the squares of the fit errors) are: [-4.3433 89.2198], 800.9071; [-3.3782 50.4837], 60.9364; [-2.6172 44.4502], 131.6114.

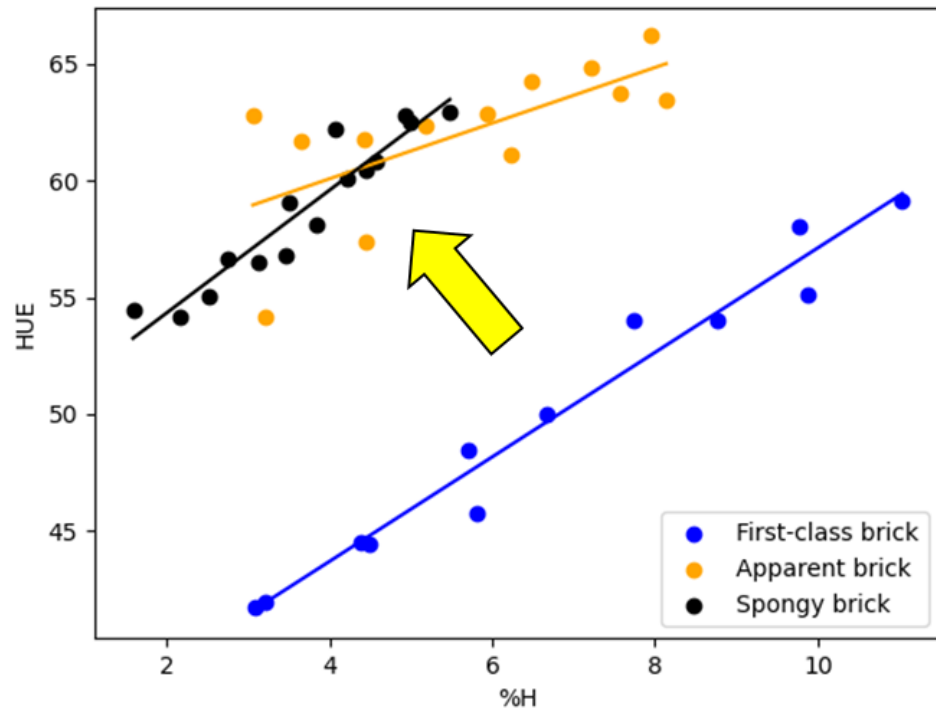


**Figure 28.** Graph illustrating the variations in moisture percentage with respect to hue (*HSI* format). Each color represents a specific type of brick. The arrow indicates the direction in which the permeability and the size of the voids increase. The coefficients of the lines and residuals (the sum of the squares of the fit errors) are: [2.2362 34.7470], 13.9864; [1.19088 55.3053], 65.6411; [2.6254 49.0763], 13.6402.

The *HSI* format is used to define the color vector with set components: hue, saturation, and intensity. It has a certain relationship to the Munsell color system, which is used for soil classification and allows a precise and standardized description of the colors present in the terrain. Developed by Albert H. Munsell [36] in the early 20th century, this scale provides a numerical and alphabetical notation combining hue, value, and chroma to uniquely define each color. In geology, color formats are used to characterize materials, identify horizons, and evaluate soil quality [37–39]. The scale’s internationally recognized character ensures consistent and comprehensible communication, making it a fundamental pillar in soil study research. Hue refers to the attribute that characterizes pure color. Saturation relates to the mixture of color with white. Intensity corresponds to the level of gray in a black-and-white image. The advantage of using the *HSI* format lies in its approximation to human color perception and interpretation. Since the eye detects some color differences based on varying levels of water content, it is expected that the water content in a brick sample is more closely related to hue than to intensity, saturation, or other attributes of the different color formats [33]. Figure 28 illustrates how the moisture percentage varies with respect to hue in the *HSI* format, considering different types of bricks. As with Figure 27, the same size of pixel was used in all the cases studied, and the experimental setup remained consistent.

Regarding the estimation of hydraulic diffusivity, this can be determined using the following equation [40–42]:

$$S_w = \operatorname{erfc}\left(\frac{Z}{2\sqrt{\alpha t}}\right) \tag{4}$$

where  $S_w$ ,  $Z$ ,  $\alpha$ , and  $t$  represent the water saturation, the height of the invasion front (in the examples presented here, the rise of the invasion front is nearly uniform, except in the case of the so-called spongy brick), hydraulic diffusivity, and time, respectively. It should be noted that Equation (4) represents an approximation, which may be insufficient in certain cases [43], in particular, in the presence of coupled processes [43]. The influence of gravity

is not accounted for in the derivation of Equation (4). The function  $erfc$  corresponds to the complementary error function, which is commonly used in the fields of probability and statistics. Hydraulic diffusivity ( $\alpha$ ), sometimes also referred to as the coefficient of hydraulic diffusion, is a parameter that describes the rate at which water moves through a porous medium. It is a fundamental property in hydrogeology and geotechnics, as it influences the soil's ability to transport and retain water, as well as the recharge and discharge of aquifers. Hydraulic diffusivity is expressed in units of area per time (typically recorded in square meters per second,  $m^2/s$ ), and its value depends on the porosity, permeability, and tortuosity of the medium. Water saturation ( $S_w$ ) in bricks refers to the amount of water that a brick can absorb or retain in its structure.

Assuming  $H \approx BVW$  (the percentage of the brick's volume occupied by water), moisture can be related to  $S_w$  using the following equation [34]:

$$H = S_w \varphi \quad (5)$$

where  $\varphi$  is the porosity of the sample. To illustrate the procedure used to obtain hydraulic diffusivity, consider the case of the second-class brick, where the height of the invasion front is  $Z = 6$  cm and  $H = 0.0611$ . In ceramic bricks, the porosity ( $\varphi$ ) ranges from 10% to 50% [7]. The time that elapsed from the start of the experiment until the invasion front reached a height of 6 cm was 20 min.

Assuming a porosity of 15% for the brick, and using the previously mentioned parameters, the water saturation is determined from Equation (5) as  $S_w = erfc(u) = H/\varphi = 0.0611/0.15 = 0.407$ . From tables corresponding to the  $erfc$ , where  $erfc(u) = 0.407$ , it follows that  $u = 0.594$ . Consequently, it can be deduced that  $0.594 = Z/(2\sqrt{\alpha t}) = 6/(2\sqrt{20\alpha}) = 0.67/\sqrt{\alpha}$ . Solving for hydraulic diffusivity,  $\alpha = (0.67/0.594)^2 = 1.27 \text{ cm}^2/\text{min}$ . Thus, the hydraulic diffusivity obtained from Equation (4) is  $\alpha = 2.11 \times 10^{-6} \text{ m}^2/\text{s}$ .

Hydraulic diffusivity can vary within the same sample, especially if the brick has structural heterogeneities or variations in porosity. The effective hydraulic diffusivity values for first-class, second-class, apparent, and spongy bricks, assuming  $\varphi = 30\%$  and  $Z = 6$  cm, are the following:  $\alpha = 0.311 \times 10^{-6} \text{ m}^2/\text{s}$ ,  $\alpha = 0.923 \times 10^{-6} \text{ m}^2/\text{s}$ ,  $\alpha = 1.68 \times 10^{-6} \text{ m}^2/\text{s}$ , and  $\alpha = 1.6 \times 10^{-6} \text{ m}^2/\text{s}$ .

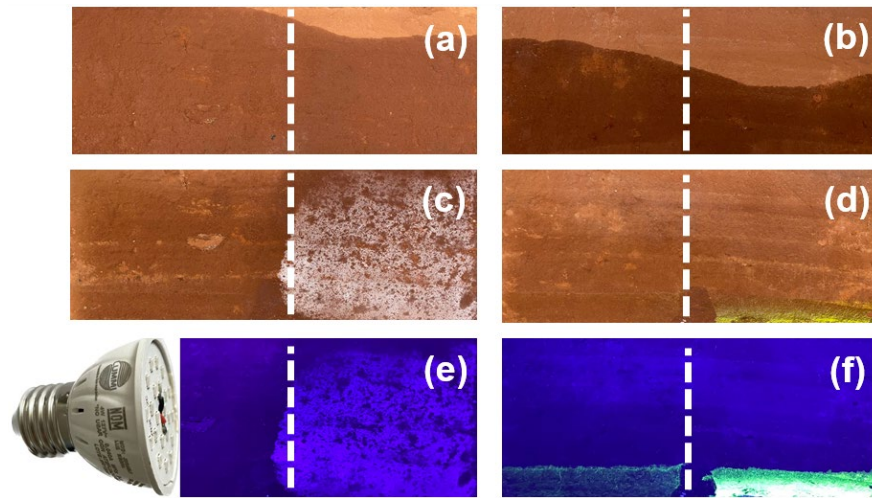
For the estimation of hydraulic diffusivity in the spongy brick type, those bricks with the most uniform invasion fronts were selected.

Different digital photography formats, such as  $HSV$ , can provide indirect information about the type of fluid invading a particular brick. The distinction between the  $HSV$  values of images obtained using UV light, showing a brick containing chlorides and one that does not, will be noticeable in a visual representation (Figures 29 and 30).

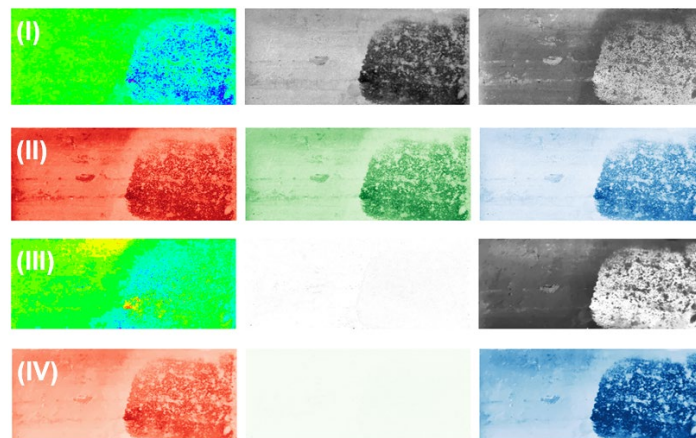
The color range exhibited by a brick with chlorides differs from one without this substance, due to the interaction of chlorides with light, leading to reflection and absorption effects that alter the material's appearance. This discrepancy in  $HSV$  values can be useful for visually detecting areas that are potentially influenced by chlorides. The tracking of chloride ions in a brick can be indirectly visualized through a simple experiment that involves inducing the capillary rise of water combined with aniline ( $C_6H_5NH_2$ ) and sodium chloride in the brick (Figure 31). This results in the appearance of layers marked by different colors—a type of chromatography that is associated with ion movement, wherein lighter ions advance further distances [44].

Figure 31 illustrates three distinct stages of efflorescence evolution: (a) early stage, (b) intermediate stage, and (c) advanced stage. In the early stage, the invasion front is clearly

visible, along with the stratification of ions indicated by the different colors. Figure 31 also demonstrates that ions travel faster in some regions of the brick.



**Figure 29.** Images showing: (a) a brick in which pure water is ascending in the first half of the image, and water with *NaCl* is ascending in the other half; (b) a brick in which pure water is ascending in the first half of the image, and water with fluorescent dye is ascending in the other half; (c,d) images illustrating the presence of efflorescence and fluorescence, respectively; (e,f) images corresponding to the UV images of (c,d).



**Figure 30.** Row (I) corresponds to the *HSV* images of image (c) shown in Figure 29. Row (II) corresponds to the *RGB* images of image (c) shown in Figure 29. Row (III) corresponds to the *HSV* images of UV image (e) shown in Figure 29. Row (IV) corresponds to the *RGB* images of UV image (e) shown in Figure 29.



**Figure 31.** Cont.

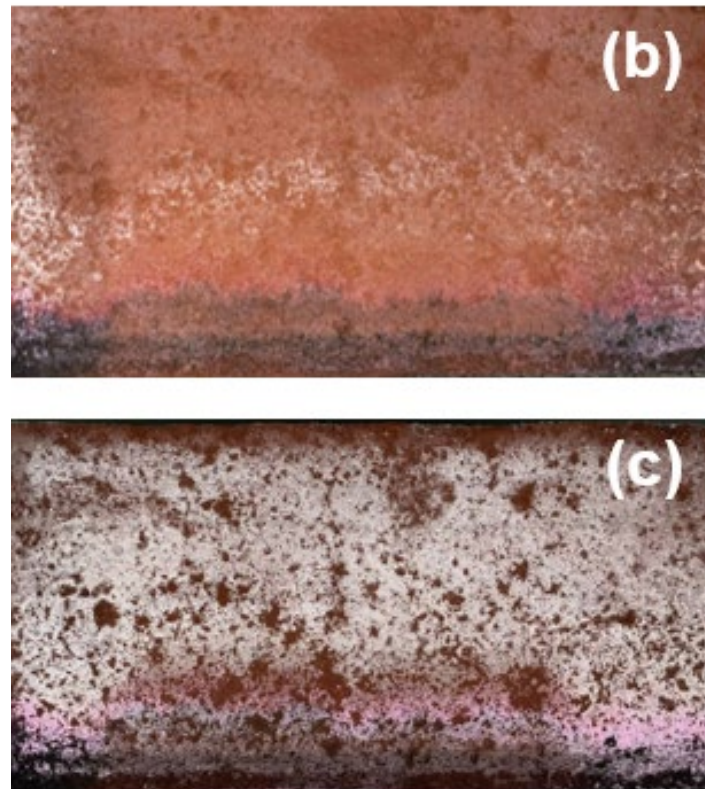


**Figure 31.** Evolution of efflorescence. Stages (a–c) are described in the text.

### 6.2. Specific Surface and Porosity

In well-sorted granular systems, the specific surface area decreases with increasing porosity, as demonstrated by both digital experiments and theoretical models [45]. However, this relationship can be reversed in systems with binary or more complex grain size distributions [45]. In sandstone and carbonate samples with low to medium porosity, the specific surface increases as the porosity rises. In contrast, granular samples exhibit the opposite behavior [45]. This behavior can be modeled using hollow ellipsoids immersed within the mineral matrix. The grains can also be modeled as solid ellipsoids situated in the otherwise vacant pore space. Considering that a particular material is composed of identical grains denoted by ellipsoids, the specific surface area ( $S$ ), which is defined as the ratio of the surface area of all grains to the volume of the pack, can be expressed as follows [45]:

$$S = 6(1 - \varphi) \left( \frac{a^{-p} + b^{-p} + c^{-p}}{3} \right)^{1/p} \quad (6)$$

where  $a$ ,  $b$ , and  $c$  correspond to the semi-axes of the ellipsoid that defines each grain. If these semi-axes are equal, the expression defined above is simplified to:

$$S = 6 \frac{(1 - \varphi)}{a}. \quad (7)$$

Figure 32 presents a plot with the vertical axis representing the specific surface area and the horizontal axis representing porosity. In this figure, two scenarios are presented that correspond to: (a) a material containing spherical grains with the radius  $a = 150 \mu\text{m}$ , and (b) a material that contains grains with an ellipsoidal form and semi-axes of  $a = 750 \mu\text{m}$ ,  $b = 610 \mu\text{m}$ , and  $c = 450 \mu\text{m}$ . Scenario (a) could represent the first- and second-class bricks, while scenario (b) may correspond to the apparent and spongy bricks, respectively. These scenarios are shown in the colors blue and black, respectively. When small particles fill the pores within a large-particle framework, the specific surface area ( $S$ ) increases as the

porosity ( $\phi$ ) decreases. Conversely, when large particles are dispersed within a continuum of smaller particles, fewer large particles result in higher porosity ( $\phi$ ) and a greater specific surface ( $S$ ). As previously mentioned, in uniform particle packs,  $S$  decreases with increasing  $\phi$  [45].

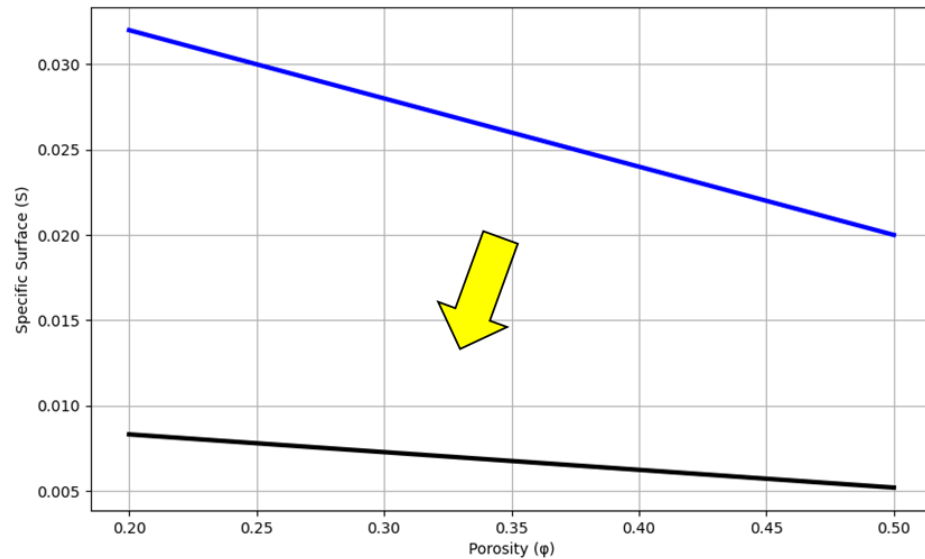


**Figure 32.** The vertical and horizontal axes represent the specific surface and porosity. The colors blue and black correspond to the values of two types of materials, the characteristics of which are described in the main text. In this example,  $p = 1$ . The arrow indicates the direction in which the grain size increases, and the shape of the grains becomes more ellipsoidal.

### 6.3. Microscopic Images

The following equipment was used to study the samples: (a) a binocular stereoscopic microscope with a focal objective ranging from 0.7 to 11.5 $\times$ ; (b) a scanning electron microscope (SEM) with an energy-dispersive spectroscopy (EDS) detector; and (c) a reflected-light petrographic microscope. The microscope images are shown in Figures 33–35.

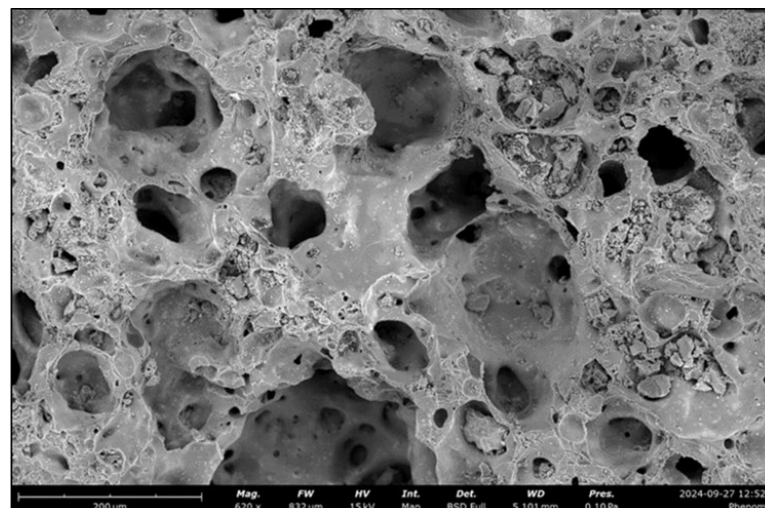


**Figure 33.** Spongy brick sample. Energy-dispersive X-ray spectroscopy (EDS) analysis of the finest component reveals a composition predominantly consisting of oxygen (O; 45.9%), silicon (Si; 22.9%), aluminum (Al; 18.5%), iron (Fe; 6.5%), and potassium (K; 2.9%), with smaller amounts of magnesium (Mg; 1.7%), calcium (Ca), and sodium (Na; 1.5%). This analysis suggests that the clayey material may

generally consist of quartz, feldspar, aluminosilicates, and phyllosilicates. The detritus is primarily composed of quartz, feldspar, hematite, and fragments of quartz-rich rocks, with particle sizes ranging from 40 to 8000  $\mu\text{m}$ . A significant portion exhibits reddish tones, tinted by the presence of iron oxide. The matrix consists of an aggregate formed by quartz, feldspar, and a binder that is likely composed of aluminosilicates and phyllosilicates. The coloration varies, depending on the observed area. The material exhibits abundant porosity, with pore diameters ranging from 100 to 4000  $\mu\text{m}$  and depths reaching up to 5000  $\mu\text{m}$ . These cavities are characterized by rounded, irregular, ovoid, and elongated shapes, often showing orientation. The SEM images reveal the presence of primary pores, which, in turn, contain subordinate, smaller interconnected pores.

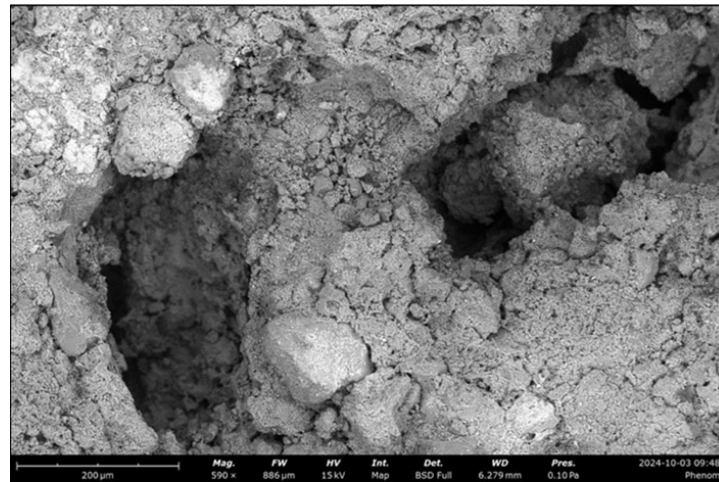


**Figure 34.** Apparent brick sample. Energy-dispersive X-ray spectroscopy (EDS) analysis of the finest component reveals a composition predominantly consisting of oxygen (O; 55.5%), silicon (Si; 16%), aluminum (Al; 16.3%), iron (Fe; 6.9%), and potassium (K; 2.3%), with smaller amounts of magnesium (Mg; 1.5%), calcium (Ca), and sodium (Na; 1.5%). The detritus appears subangular, with tabular, prismatic, or irregular (fragmented) shapes ranging in size from 40 to 6000  $\mu\text{m}$  in diameter. Smaller particles are primarily quartz, feldspar, and hematite, with disseminated traces of pyrite, while larger particles generally consist of fragments of heterogeneous, typically quartz-rich rocks. The matrix has a homogeneous, very fine-grained, submicroscopic structure (<3  $\mu\text{m}$ ) with a reddish hue, acting as a cementing agent to support the sandy component. The voids are regular cavities that are homogeneously distributed, with rounded shapes that are frequently oval and irregular, ranging in size from 500 to 3000  $\mu\text{m}$  in diameter.



**Figure 35.** First-class brick sample composed of clasts of varying sizes, ranging from 60 to 7000  $\mu\text{m}$ , prominently featuring minerals and fragments of heterogeneous rock. The minerals are primarily

represented by quartz (Qz), feldspar, and hematite. A mixture of clays forms the base or matrix of the brick, exhibiting a pale orange color. This matrix is submicroscopic in size ( $<3 \mu\text{m}$ ) and serves as the paste responsible for agglomerating the sandy material and fragments of rock (FgR), acting collectively as a binding agent and thereby providing cohesion to the material. The sample is characterized by some porosity, featuring rounded, ovoid, or elongated shapes, with diameters ranging from 80 to 6000  $\mu\text{m}$  and depths of up to 5000  $\mu\text{m}$ . The larger voids may exhibit subordinate smaller voids, which could indicate, in several instances, partially interconnected porosity. It should be noted that the observed porosity in this brick may be partially due to the sample-cutting process.

## 7. Discussions

The variability in the permeability of masonry units, as discussed above, is a critical issue in the construction industry that warrants significant attention and may lead to substantial debate [7]. Permeability can vary across the different areas of a masonry unit due to several factors, including firing variability, material composition, compaction, and manufacturing defects. Firing variability can cause the inconsistent curing of bricks, resulting in differential porosity and permeability [7]. The material composition, particularly the type and proportion of clay, additives, and other raw materials, is fundamental in determining the permeability characteristics of the units [7]. Compaction during the manufacturing process also affects the density and uniformity of bricks; inadequate compaction can lead to higher permeability [7]. Additionally, manufacturing defects, such as cracks or incomplete formations, can exacerbate these issues. Variations in these factors can significantly impact the quality standards of masonry units. Highly permeable units can allow moisture ingress, leading to a cascade of problems including structural deterioration, efflorescence, and mold growth [6]. These issues not only compromise structural integrity but also affect the aesthetic and functional aspects of buildings. Furthermore, the presence of mold in buildings poses serious health risks, contributing to respiratory problems and other health issues for the occupants [6]. These concerns underscore the importance of adopting best construction practices and striving to create healthy and comfortable indoor environments [6]. They also highlight the need for stringent regulations and standards governing the manufacture of masonry units to ensure consistency and quality [6]. Effective quality control measures, such as regular permeability testing and adherence to standardized manufacturing processes, are essential for mitigating these issues [6].

Table 2 presents the total water absorption values for various masonry units. These values demonstrate that the units comply with the NMX-C-404-ONNCCE-2012 standard [32], which sets a maximum allowable water absorption criterion of 23%. This compliance indicates that the masonry units meet the necessary quality standards for water absorption, ensuring their suitability for construction purposes. Irregular water saturation typically refers to conditions in which the water content within a specific medium, such as a masonry unit or a porous rock, is not uniformly distributed. Instead, the water is concentrated in localized or discontinuous regions within the material. This phenomenon can arise due to several factors, including inconsistencies in material composition, varying degrees of porosity, and differences in compaction during manufacturing. Irregular water saturation can significantly impact the performance and durability of masonry units, leading to potential issues such as uneven structural stress, localized deterioration, and the compromised integrity of the construction [7]. Understanding the patterns and causes of irregular water saturation is crucial for improving the manufacturing processes and quality control measures of masonry units. By addressing these factors, manufacturers can enhance the uniformity and overall performance of the units, thereby contributing to the longevity and stability of masonry structures [7]. Moreover, further research and advanced testing methods are essential to accurately assess and mitigate the effects of irregular water saturation in masonry materials.

**Table 2.** Total absorption of water over a 24-h period.

BRICK	TOTAL ABSORPTION OF WATER
FIRST CLASS	18.19%
SECOND CLASS	17.17%
APPARENT	16.18%
SPONGY	13.8%

Changes in color intensity in the image formats can serve as indicators of moisture-affected areas in the masonry units. This visual information is highly relevant for building inspection and quality control applications, aiding in the detection and assessment of moisture problems. In *RGB* images, color variations may be associated with differences in surface texture and composition, which can influence the permeability of the material. These variations can provide preliminary insights into potential areas of concern.

Furthermore, utilizing alternative color spaces such as *YUV*, *HSV*, and *HSI* can enhance the analysis. These color spaces offer distinct advantages by providing information on luminance, hue, saturation, and value, which data can be instrumental in identifying permeable areas within the masonry units. For instance, the *YUV* color space separates luminance (brightness) from chrominance (color information), making it easier to detect subtle changes in moisture levels. Similarly, the *HSV* and *HSI* color spaces, which emphasize hue, saturation, and intensity, can help in distinguishing between moist and dry regions more effectively. However, it is crucial to validate the moisture percentage estimates derived from photographic analysis with measurements obtained using other established techniques, namely, electrical resistance and neutron scattering. Cross-validation with these methods ensures the accuracy and reliability of the moisture detection process, thereby enhancing the credibility of the visual inspection results.

The use of digital image processing driven by artificial intelligence presents a promising approach for estimating moisture percentages in fired red bricks, thereby aiding in moisture management and quality control.

The methodology described in this study is intended to complement, rather than replace, traditional moisture measurement techniques. By leveraging AI algorithms, this image processing method has demonstrated its reliability, as evidenced by the close agreement between the segmented images and reference photographs. A key aspect of this methodology is the identification of moisture clusters through the combined application of principal component analysis (PCA) and K-means clustering. PCA helps in reducing the dimensionality of the image data, highlighting the most significant features, while K-means clustering can effectively group similar data points, thereby identifying those regions with varying moisture content.

The results of this study indicate that this AI-driven image processing technique can significantly impact the evaluation of moisture in structures. The ability to accurately and efficiently detect moisture clusters can lead to better-informed decisions in the construction and maintenance of buildings.

Using relative brightness differences as a form of “internal normalization” is important for minimizing the effects of lighting variations across an image. This technique relies on the assumption that changes in lighting impact all areas of the image uniformly.

By focusing on relative brightness differences rather than absolute values, the influence of variable lighting conditions can be mitigated. In the context of images with different pixel sizes, brightness percentages can vary, due to the inherently fractal nature of image processing using different pixel sizes.

Fractals are characterized by self-similarity across different scales, meaning that an object displaying fractal properties will exhibit similar patterns at various levels of magnifi-

cation. This self-similarity is relevant when analyzing digital images, especially when pixel sizes and image resolutions are adjusted.

For instance, natural elements such as coastlines demonstrate fractal characteristics, showing complex, irregular shapes that persist at multiple scales. When measuring geometric properties like the length or area of such fractal objects, the results can differ based on the scale at which measurements are taken.

This scale-dependent variation is a consequence of the fractal dimension, which quantifies the complexity of an object [34]. The choice of pixel size and image resolution plays a significant role in how these physical properties are represented and measured. Internal normalization through relative brightness differences helps account for variations in lighting, which could facilitate a more consistent analysis of fractal-like structures in digital images.

In the realm of construction material evaluation and architectural heritage preservation, accurately identifying the substances within masonry units is paramount. The presence of chlorides, for instance, can greatly influence the integrity and longevity of these structures [6]. Traditional methods of detection often grapple with uncertainties that can compromise the accuracy of the results.

Advancements in digital photography and image processing offer promising solutions. Digital photography formats such as *RGB* (red, green, and blue), *HSV* (hue, saturation, and value), and *HSI* (hue, saturation, and intensity) can help to reduce any uncertainties in the identification of moisture percentages within masonry units. Each of these formats offers unique advantages in capturing and analyzing the interactions between light and materials.

The *RGB* color model is fundamental in digital imaging, representing images in terms of the primary colors of light. By analyzing the intensity of red, green, and blue components, we can infer the presence of chlorides, which typically alter the color balance of the material.

The *HSV* color model separates the chromatic content (hue) from the intensity and purity (saturation and value). This separation allows for a more intuitive identification of color changes caused by chlorides. Similar to *HSV*, the *HSI* color model provides a representation that aligns closely with human perceptions of colors. By focusing on hue, saturation, and intensity, this model facilitates the detection of subtle changes in appearance due to chlorides.

Similar to *HSV*, the *HSI* color model provides a representation that aligns closely with human perceptions of colors. By focusing on hue, saturation, and intensity, this model facilitates the detection of subtle changes in appearance due to chlorides. Chlorides can cause noticeable changes in the appearance of masonry materials, such as discoloration or efflorescence. By utilizing different digital photography formats, these changes can be quantified and analyzed, providing a more accurate assessment of the presence of chloride. Beyond chloride detection, these digital photography formats are instrumental in estimating the moisture percentage within masonry units. Moisture can affect the material's appearance, and by leveraging *RGB*, *HSV*, and *HSI* values, we can derive the correlations between visual changes and moisture levels. This capability is essential for evaluating the condition of construction materials and preserving architectural heritage.

Beyond their theoretical implications, these findings have practical value, particularly for quality control in traditional and eco-friendly brick construction. The percentage of luminosity was observed to be highly sensitive to slight inclinations in first-grade bricks. In contrast, hue values demonstrated a better fit to a single regression line and were less affected by environmental variations, with the exception of some strong outliers. In experiments considering soil-oil-water systems, the hue (*HSI* system) of the transmitted light has been found to correlate directly with the water content in porous media [33]. This parameter offers a high-resolution measurement of both the water and oil contents

in transient flow fields [33]. The *HSI* format is similar to the Munsell color chart used for soil classification. As mentioned before, this specifies a color using hue, saturation, and intensity [33]. Hue describes the pure color, saturation indicates the degree of dilution with white, and intensity corresponds to the gray level [33]. The *HSI* format aligns with human color perception, making it useful for interpreting color differences. Since these differences are noticeable to the human eye in varying water and oil contents, water content is expected to correlate more directly with hue than with other color formats [33]. However, certain strong outliers were noted, likely associated with drastic light absorption and fluorescence. These hue anomalies could be attributed to several factors, including: (a) the presence of heterogeneities like rock fragments that can contain grains of quartz; and (b) the presence of genuine clays that, in combination with water, could be capable of absorbing light. Chemical reactions may occur during the capillary rise of water in the brick. The clays in question could exhibit honeycomb-like molecular structures, further influencing their absorption characteristics.

Materials and minerals interact with electromagnetic radiation by reflecting and absorbing it in a manner that varies with the radiation's wavelength. These interactions are depicted in the reflectance spectra, which highlight the differences in reflection and absorption across various wavelengths [46]. The mechanisms responsible for the absorption of electromagnetic radiation operate at the molecular and atomic levels and can be categorized into two primary types: electronic and vibrational processes [46]. Electronic processes involve the absorption of photons by individual atoms or ions within minerals at specific wavelengths, leading to distinctive absorption features in the reflectance spectra [46]. For example, the absorption of certain wavelengths by iron atoms in oxides and hydroxides results in these minerals exhibiting a red color [46]. Vibrational processes, on the other hand, involve the absorption of photons by molecular bonds, which induces vibrations within the molecules. This type of absorption is characteristic of the bonds in materials such as clay minerals, where the molecular structure absorbs specific wavelengths, contributing to the material's overall spectral properties [46]. Both electronic and vibrational processes are critical for understanding the optical behavior and colors of minerals and materials (including gas and liquids, which could be situated around the grains of the materials).

Efflorescence, a common issue in masonry units, results from the deposition of soluble salts on the surface of bricks [6]. Detecting and analyzing efflorescence is crucial for maintaining the structural integrity and aesthetic value of masonry constructions [6]. This study presents a methodology leveraging UV light, digital imaging, and AI to address the identification of areas affected by efflorescence. Efflorescence can be efficiently detected in fired red bricks through the application of UV light, capitalizing on the fluorescence properties of many soluble salts. According to Pirson [47], salts such as calcium carbonate and sodium chloride exhibit fluorescence under UV light, emitting a visible light that facilitates their detection.

The proposed process comprises the following steps: (a) a UV light source is employed to illuminate the surface of the masonry unit. UV light's ability to excite the soluble salts present in the material's pores makes it an effective tool for highlighting efflorescence. Ensuring an optimal environment with minimal ambient light enhances the visibility of the fluorescence. (b) Under UV illumination, incipient efflorescence becomes visible, due to the fluorescence of the soluble salts. This fluorescence aids in the early detection of efflorescence, which might not be easily discernible under normal lighting conditions. (c) Photographic documentation of the illuminated surface is crucial for detailed analysis. High-resolution images captured under UV light can be digitally processed to enhance the visibility and contrast of the efflorescence. (d) Once photographic images of efflorescence are obtained, unsupervised learning can be applied to analyze the data. AI algorithms can

identify the presence, size, and distribution of efflorescence within the masonry unit. This automated analysis provides a comprehensive understanding of the extent and severity of the efflorescence, enabling more informed decisions for remediation and preservation. The integration of UV light detection, digital photography, and AI analysis can represent a significant advancement in the study of efflorescence in fired red bricks. This methodology enhances the accuracy of the analysis, which is critical for effective maintenance and preservation strategies. Future research should focus on refining the AI algorithms employed and exploring the fluorescence properties of different salts to broaden the applicability of this technique.

Ion stratification within masonry units results from the differential movement of ions as water ascends through the material, carrying dissolved substances with it. This process bears a resemblance to chromatography, where substances are separated based on their movement through a medium. Understanding ion stratification is crucial for comprehending the diffusion processes and material behavior in masonry. Kovats [44] draws a parallel between ion stratification in sand saturated with brine and chromatographic separation. In chromatography, substances are separated based on their interaction with a stationary phase and their relative mobility. Similarly, in masonry units, ions stratify according to their size and charge, with the lighter ions traveling further and faster than heavier ones.

This analogy provides a framework for analyzing ion movement and diffusion within the material. The experimental setup, depicted in Figure 31, involved the use of a 15% *NaCl* solution to study ion stratification. The steps followed in this experiment are as follows: (a) a masonry unit was saturated with a 15% *NaCl* solution, mixed with aniline, to indirectly observe the movement of ions; (b) the solution was allowed to ascend through the masonry unit, simulating natural water movement and ion transport; (c) as the solution ascended, the stratification of ions occurred, with lighter ions traveling longer distances than heavier ones. This stratification was visualized using aniline, which highlighted the different layers formed due to varying ion migration rates. (d) The resulting stratified layers were analyzed using AI and image processing. This experiment demonstrated how ion stratification can reveal insights into the diffusion processes and the behavior of ions within the masonry unit. The experiment illustrated that the lighter ions in the 15% *NaCl* solution traveled longer distances within the masonry unit compared to heavier ions. This stratification mirrors chromatographic separation, confirming the analogy and providing a valuable tool for studying diffusion processes in masonry [44].

The observed layers offer insights into how ions interact with the masonry material, and how they influence the overall diffusion behavior and the adsorption process. Adsorption is the process by which ions, atoms, or molecules adhere to the surface of a solid. In the case of clay, chloride ion adsorption can occur due to the specific surface properties of the clay [47]. Chloride ions, which are negatively charged anions, can be attracted to positively charged sites on the clay surface due to electrostatic interaction.

This adsorption process is significant in the chemistry of material that contains clays [47]. The ions that adsorb onto the clay surface can be important in ion exchange processes [47]. The negatively charged ions, corresponding to chlorine, adhere to the surface of the clay [47], grouping together and forming specific structures [47]. These structures can capture atomic particles and lead to chemical reactions, which, in turn, can induce crystallization [47].

The adsorption of chloride ions on clay surfaces is somehow linked to the concept of the exclusion zone (EZ) layer [48], a key phenomenon in water science. The EZ layer refers to a structured, quasi-crystalline phase of water that forms near hydrophilic surfaces, distinct from bulk water, and excludes particles and solutes. This process underscores the critical role of surface chemistry in governing the behavior of water and ions at material interfaces,

such as those found in clay. The interplay between a specific surface, porosity, permeability, the EZ layer, ion adsorption, and light absorption reveals a complex interaction between material properties and water behavior near surfaces. The specific surface ( $S$ ) is pivotal in EZ layer formation, as a larger specific surface facilitates greater interaction with water molecules, leading to a more extensive EZ layer. This is particularly relevant with porous materials, where the specific surface significantly contributes to EZ development.

Porosity and permeability further modulate this relationship: higher porosity allows more water to occupy the material, while permeability influences the water movement within it. The EZ layer can, in turn, alter both porosity and permeability by restructuring water near the surfaces, potentially reducing flow in highly permeable materials. UV light absorption plays a crucial role in enhancing EZ layer formation by providing the energy needed for structuring water molecules [48]. Consequently, materials with a high specific surface and optimized porosity and permeability can exhibit significant changes in their interaction with water and light, with the EZ layer serving as a mediator influencing these properties.

It should be mentioned that the color of a red brick has a notable impact on the absorption of visible light by those pores saturated with water. Red bricks typically contain pigments or iron oxides that reflect red wavelengths while absorbing other colors within the visible spectrum, such as blue and green. When the brick's pores are saturated with water, the interaction between light and the brick's color becomes more complex. Water absorbs light across the visible spectrum, with a higher absorption in the blue region due to its intrinsic properties. The red coloration of the brick, however, affects the light penetrating into these pores by reflecting the blue and green wavelengths away. As a result, the overall light absorption characteristics of the water in the pores are influenced by both the water's absorption properties and the brick's color (which depends on the ingredients), thereby altering the light spectrum. Percentages derived from images of bricks containing water are presented in Figure 36. In this figure, the subscripts 1, 2, P, and A denote the following: first brick, apparent brick, hue ( $HSI$  format) of the first brick, and hue ( $HSI$  format) of the apparent brick, respectively.

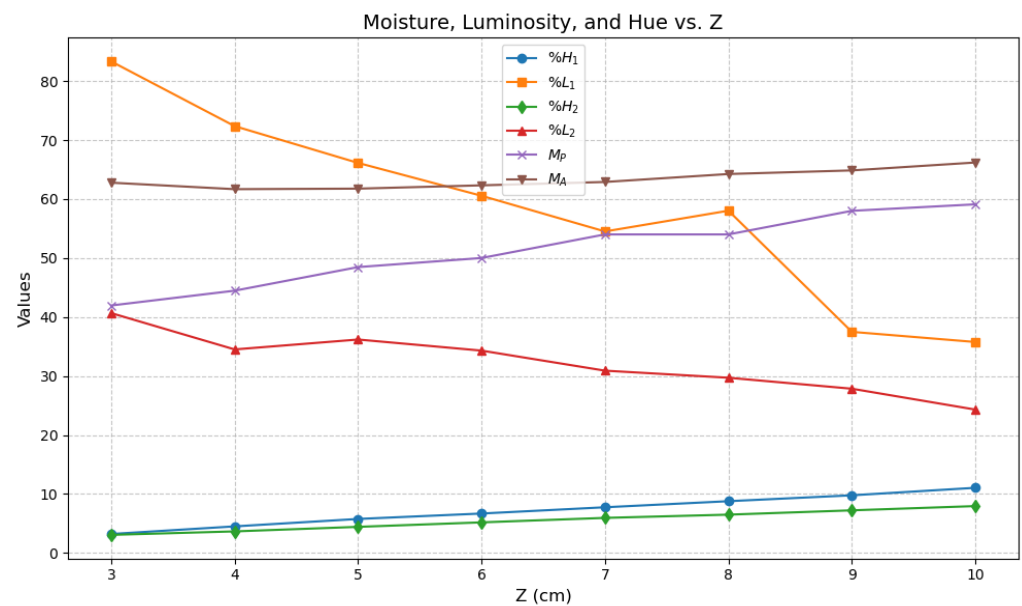


**Figure 36.** Moisture percentage ( $\%H$ ), percentage of luminosity ( $\%L$ ), and hue of the wet region ( $M$ ). Hue values ( $HSI$  format) are given in degrees.

During the capillary rise of water in a red brick, chemical reactions between the water and the brick can generate various gases. Key gases that may be produced include carbon

dioxide from carbonate reactions and, potentially, hydrogen from redox reactions involving metal components in the brick. If the brick contains metals such as iron or aluminum, hydrogen gas could be generated through these redox reactions. Notably, hydrogen absorbs light, primarily in the ultraviolet (UV) and far-infrared (IR) regions of the spectrum, rather than in the visible light range. Conversely, chloride-containing compounds in the brick could facilitate the generation of chlorine gas, which has the ability to absorb visible light.

Salts cause damage to construction materials and can lead to efflorescence on walls and slabs. This has increased research interest in understanding chloride transfer phenomena in porous materials, such as bricks. It is worth noting that there is still a scarcity of information on this topic in the specialized literature, particularly regarding the diffusion coefficients of salts in different types of brick. The diffusivity coefficient for sodium chloride in fired red bricks can be estimated using Fick's law through regression techniques [49].

The diffusion equation describes how energy (in the form of heat) or mass (in the form of moisture) is transferred from regions of high concentration to regions of low concentration [50]. The direction of transfer is driven by the temperature gradient (for heat) or the moisture concentration gradient. The diffusion coefficients ( $\alpha$  for moisture and  $D$  for heat) are critical parameters. These determine the rate at which the studied quantity (heat or moisture) diffuses through the medium. High values of these coefficients indicate a greater rate of diffusion [40]. For an estimation of the hydraulic diffusivities of bricks, the sharp front model concept was utilized [7]. The capillary diffusivity of most porous materials exhibits substantial variation with liquid content, leading to very steep capillary absorption profiles. Consequently, it is often practical and beneficial to depict the wetted region as a rectangular or sharp-fronted profile, which is referred to as the sharp front approximation [7]. Utilizing this model allows for relatively simple mathematical descriptions of the numerous wetting processes [7]. We also assume that the water content in the bricks is proportional to the products of porosity and water saturation [34]. The estimated effective hydraulic diffusivity values, calculated with an invasion front height of 6 cm, align with those documented in the specialized literature. The observed variability in hydraulic diffusivity can be attributed to several factors, including porosity, the presence of microfractures, material imperfections, and contaminants. These elements influence the movement and distribution of fluids within the material, thereby affecting its hydraulic properties.

Moisture is often associated with the presence of fractures, making it a critical factor in the characterization of walls and slabs that may be compromised by differential settlement. Advanced methods for inspecting these fractures, such as digital photography, have been well-documented [51–53]; in these methods, transfer and unsupervised learning are utilized, which have demonstrated the potential of unsupervised learning for differentiating cracks from noise in images of concrete [52]. However, the use of drone-acquired digital photographs to study moisture in slabs and walls represents a novel approach that can significantly enhance the monitoring and management of architectural challenges [54,55]. The methodology presented in our study can combine the multi-spectral imaging capabilities of drones with unsupervised learning. This approach can be further improved by the incorporation of InSAR (interferometric synthetic aperture radar) imaging [46]. InSAR works by using the radar signals emitted from satellites or aircraft to capture images of the Earth's surface. By comparing two or more radar images taken from slightly different positions or at different times, InSAR can detect small changes in the Earth's surface, such as those caused by infrastructure deformation [46]. InSAR imaging provides valuable data on surface deformation over time, which can reveal subtle ground movements that are indicative of deeper structural issues [56]. Cracks observed in buildings due to subsidence may facilitate the propagation of moisture, which, in turn, could compromise the struc-

tural and bioclimatic integrity of walls and roofs. Thermal imaging is particularly useful in detecting temperature variations that correlate with moisture levels and underlying structural anomalies. UV imaging offers the ability to identify surface irregularities and microfractures that may be invisible in standard or thermal images. By combining these imaging techniques, we propose a comprehensive and detailed method for assessing structural integrity. This approach can not only improve the accuracy and reliability of moisture and fracture detection but also offer a tool for the ongoing management of architectural structures. However, the methodology's applicability is influenced by certain limitations, particularly in environments with highly variable lighting, which can impact image-based moisture estimates.

## 8. Conclusions

1. The *RGB*, *YUV*, *HSV*, and *HSI* formats provide detailed information about luminance, hue, saturation, and value, playing an important role in the reduction of uncertainties in the detection of areas with moisture and permeability issues. *RGB* and *HSI* formats are particularly useful in the mitigation of uncertainties during the detection of chlorides, which tend to darken the brick over time more markedly than water after their introduction into the sample. At later stages, efflorescence begins to develop.
2. The invasion of water lasted longer in first-grade bricks. Both first-grade and second-grade bricks exhibited the highest levels of moisture. However, in bricks treated with waterproofing agents based on soap and alum fragments, the partial moisture content remained extremely low. Bricks fired at lower temperatures exhibit greater expansion, higher water absorption, and a greater susceptibility to deterioration compared to those fired at higher temperatures [57].
3. The percentage of luminosity was found to be sensitive to slight inclinations of the first-grade brick, while the hue values fitted a single regression line better, being less sensitive to various environmental variations. This was except for certain outliers that could be associated with drastic light absorptions and fluorescence, likely due to the combined influence of various factors, such as: (a) the presence of rock fragments that could contain grains of quartz; and (b) the presence of genuine clays that can absorb various components generated in chemical reactions (which may occur during the capillary rise of water in the brick); these clays could exhibit honeycomb-like molecular structures.
4. The percentage of luminosity and hue were inversely and directly correlated, respectively, with the percentage of moisture.
5. The incorporation of a sodium chloride solution combined with aniline in the brick allows for indirect visualization of the movement of chloride ions, offering a chromatographic perspective.
6. In the spongy brick, there was a noticeable increase in the rate at which water rose by capillarity. This anomalous increase in permeability is due to the following factors: (a) strong permeability: the mixture of clay with other materials like sawdust or organic matter, which burn out during firing, leaving behind a network of voids or pores within the brick, resulting in a spongy structure that is highly permeable; (b) effective sintering: the sintering process fuses the particles together [58], creating a strong, cohesive matrix that can withstand significant forces. The internal cellular structure of spongy bricks, characterized by a network of cells or pores that function as a system of small compartments, contributes to their permeability. These chambers could help in dissipating the force throughout the brick, preventing it from failing at a single point. In fact, spongy bricks are used for road surfacing and can withstand the passage of heavy vehicles. It should be mentioned that while higher firing temperatures can

- reduce permeability, the specific composition and manufacturing techniques used for spongy bricks can give rise to a highly permeable structure.
7. The scanning electron microscope (SEM) images presented in Figures 33–35 provide key insights into the pore structures of different brick types. Specifically: (a) the spongy brick exhibits a highly interconnected pore network, which significantly enhances its permeability. This interconnected structure facilitates the movement of fluids through the brick, making it highly permeable. (b) The apparent brick exhibits a partially interconnected pore system. Manufactured at a lower temperature than the spongy brick, it retains a substantial amount of “intact” clay. The presence of this clay enhances water absorption in the apparent brick relative to the spongy brick. (c) The first-class brick was produced at a lower temperature than the apparent brick, resulting in an even higher proportion of “intact” clay. This clay content significantly contributes to the brick’s water absorption capacity. Furthermore, the clay content influences the brick’s structural integrity, reducing its permeability while increasing its water retention performance. These characteristics may impact the brick’s long-term durability and resistance to environmental conditions. (d) The spongy brick, with its porous and interconnected structure, can be likened to a 3D gyroid-like assembly, similar to recent advancements in three-dimensional (3D) graphene composites [59]. In much the same way that 3D graphene materials exhibit a unique balance between strength and lightness, due to their intricate geometric arrangements, the spongy brick achieves significant mechanical resilience under both static and dynamic loads through its own complex pore structure. Much like 3D graphene, the spongy brick’s pores are not just random voids but, rather, form a highly organized network that resembles the gyroid patterns observed in advanced materials. This geometric arrangement allows for an efficient distribution of forces across the brick, enhancing its ability to bear heavy loads without structural failure. The solid material surrounding the pores in the spongy brick functions similarly to the robust carbon framework in porous graphene composites, reinforcing the brick’s ability to maintain its shape and integrity under high pressure.
  8. Insulating materials made from partitions with a gyroidal structure possess favorable characteristics for thermal insulation [60], effectively minimizing heat transfer and providing energy efficiency benefits [60]. This could be particularly useful in various applications, including the construction of bioclimatic structures, where maintaining temperature control is essential. However, it should be taken into account that the thermal conductivity of commonly used insulation materials increases with rising temperature and humidity, underscoring moisture as a critical issue in bioclimatic structures [9].
  9. In some instances, the rate of change in moisture content relative to the square root of time for the spongy brick was similar to that of first-grade brick. Given that the rate of change in moisture content relative to the square root of time followed a linear trend across all four brick types, it can be concluded that the brick fabrication process is consistent and effective.
  10. The effective characterization of efflorescence in brick can be achieved by complementing traditional techniques with the interpretation of images processed with artificial intelligence (AI) and obtained under ultraviolet light.
  11. The use of AI in image processing is fundamental for identifying areas affected by moisture. The principal component analysis (PCA) technique simplifies the detection of regions with moisture. The K-means algorithm has proven to be a useful tool for color-based data clustering; the association of light and dark colors with dry and wet regions, respectively, becomes a valuable means of interpretation.

12. Designing a kiln for the production of customized bricks is recommended, utilizing image processing and artificial intelligence to guide the production of bricks. The kiln should be engineered to create a consistent firing environment that enhances the bricks' moisture-regulating properties. This involves maintaining optimal conditions to ensure that the bricks can effectively absorb and release excess moisture, thereby regulating indoor humidity. Additionally, the bricks must be engineered to endure variable environmental conditions, thereby minimizing the degradation or adverse effects due to prolonged moisture exposure.
13. The estimated effective hydraulic diffusivity values, assuming an invasion front height of 6 cm, are consistent with the values reported in the specialized literature.
14. The methodology presented here can be applied to the study of bioclimatic housing [61,62] requiring the use of infrared and ultraviolet images. It should also be supplemented with other techniques, such as using fiber-optic sensing (DAS) to estimate moisture percentage, as demonstrated in a study of the propagation of moisture using DAS in soils by Shen et al. [63].
15. Automated image processing, driven by AI and smartphone technology, enabled the estimation of the percentage of moisture in bricks. This methodology holds significant potential for application in quality control (QC) processes within brick fabrication, ensuring that production standards are consistently met and improving the overall reliability of the final product.
16. According to the results obtained, the bricks from the community of San Agustín Yatareni, Oaxaca, comply with the NMX-C-404-ONNCCE-2012 [32] Mexican standard, with a total water absorption percentage ranging from 13.8% to 18.2%, values within the limits defined in Table 2 of this standard; this finding is verified according to the test method specified in the Mexican standard NMX-C-037-ONNCCE-2013 [31]. Regarding the moisture content, the bricks studied herein meet the requirements for use in construction projects. With this information, technical portfolios of bricks could be developed to enhance marketing and promotional efforts. These portfolios would be valuable for both local and international clients who are interested in constructing houses in Oaxaca.
17. Our study introduces an image-based approach for evaluating the moisture levels in fired red bricks. Leveraging color theory alongside AI-driven clustering, this methodology provides a promising non-destructive alternative for moisture detection. It is important to note that the proposed approach is designed to identify dampness primarily in the near-surface zone of the masonry. Future research could build upon this framework, expanding its applicability to other porous construction materials and further advancing sustainability and resilience within the industry. The integration of this approach with advanced structural integrity assessment technologies, such as LiDAR-equipped drones, LiDAR-enabled smartphones, InSAR imagery, and distributed acoustic sensing (DAS) systems, offers significant potential to improve construction practices. By harnessing these cutting-edge tools, it becomes possible to achieve a higher degree of automation in construction processes, reducing manual intervention and increasing efficiency.

**Author Contributions:** Conceptualization, A.A.R.-M.; Formal analysis, A.A.R.-M.; Investigation, A.A.R.-M.; Data curation, A.A.R.-M. and A.A.P.-R.; Writing—original draft, A.A.P.-R.; Writing—review & editing, A.P.-P.; Visualization, A.A.P.-R.; Supervision, A.P.-P. All authors have read and agreed to the published version of the manuscript.

**Funding:** This research received no external funding.

**Data Availability Statement:** Data are contained within the article.

**Acknowledgments:** The first author is grateful to SNI-CONAHCYT for its financial support. The authors also extend their thanks to Francisco Javier Cruz Velasco, Edgar Eutiquio Martínez Vásquez, Carlos Enrique Mayoral Peña, Marco Antonio Maldonado García, and two anonymous reviewers for their valuable comments and suggestions. Aida Alejandra Ricárdez-Montiel conveys her gratitude to Universidad Autónoma Benito Juárez de Oaxaca for the academic support provided during the development of her undergraduate thesis [64]. The authors extend their gratitude to the artisans of San Agustín Yatareni for their invaluable insights into the brick fabrication process, and to the Mexican Geological Service (SGM) for capturing the microscopic images.

**Conflicts of Interest:** The authors declare no conflict of interest.

## References

1. CSEG. From Seismic to Permeability Characterization: A Combined Rock Physics, BVW Modelling and Seismic Inversion Workflow. Available online: <https://cseg.ca/from-seismic-to-permeability-characterization-a-combined-rock-physics-bvw-modelling-and-seismic-inversion-workflow/> (accessed on 10 October 2023).
2. Campbell, J.W.P.; Pryce, W. *Brick: A World History*; Thames & Hudson: London, UK, 2003; Volume 1, pp. 1–320.
3. Instituto Nacional de Antropología e Historia. Mediateca INAH: Comalcalco. Available online: [https://mediateca.inah.gob.mx/islandora\\_74/islandora/object/sitioprehispanico:1718](https://mediateca.inah.gob.mx/islandora_74/islandora/object/sitioprehispanico:1718) (accessed on 6 October 2023).
4. Norman Foster Foundation. About Their Twelve Strategies for Construction [Video]. Available online: <https://www.youtube.com/watch?v=ZJ1neq3CYLQ> (accessed on 8 October 2023).
5. Cetto, M.L. *Modern Architecture of Mexico*; UNAM: Mexico City, Mexico, 2021; Volume 1, pp. 1–133.
6. USEPA. *Guide for Moisture Control in the Design, Construction, and Maintenance of Buildings*; United States Environmental Protection Agency: Washington, DC, USA, 2016; Volume 1, pp. 1–156. (In Spanish)
7. Hall, C.; Hoff, W.D. *Water Transport in Brick, Stone and Concrete*; CRC Press: Boca Raton, FL, USA, 2009; Volume 1, pp. 1–362.
8. McBurney, J.W. Masonry cracking and damage caused by moisture expansion of structural clay tile. *Proc. ASTM* **1954**, *54*, 1219–1238.
9. Wang, Y.; Liu, K.; Liu, Y.; Wang, D.; Liu, J. The impact of temperature and relative humidity dependent thermal conductivity of insulation materials on heat transfer through the building envelope. *J. Build. Eng.* **2022**, *46*, 103700. [CrossRef]
10. Zúñiga, A.; Eires, R.; Malheiro, R.; Felgueiras, H.P. The impact of sugarcane bagasse on the biological degradation of hemp concrete. *Ind. Crops Prod.* **2024**, *219*, 119075. [CrossRef]
11. Chantit, F.; El Abbassi, F.E.; Kchikach, A. Performance of compressed earth bricks reinforced with sugar industrial by-products bagasse and molasses: Mechanical, physical and durability properties. *J. Build. Eng.* **2024**, *90*, 109403. [CrossRef]
12. Hola, A. Methodology of the quantitative assessment of the moisture content of saline brick walls in historic buildings using machine learning. *Arch. Civ. Mech. Eng.* **2023**, *23*, 141. [CrossRef]
13. VanderPlas, J. *Python Data Science Handbook*; O'Reilly: Sebastopol, CA, USA, 2016; Volume 1, pp. 1–50.
14. Haykin, S. *Neural Networks and Learning Machines*; Prentice Hall: Upper Saddle River, NJ, USA, 2009; Volume 1, pp. 1–906.
15. Entrop, A.G.; Vasenev, A. Infrared drones in the construction industry: Designing a protocol for building thermography procedures. *Energy Procedia* **2017**, *132*, 63–68. [CrossRef]
16. Auer, L.; Feichtner, A.; Steinhäusler, F.; Delleske, R.; Keusch, M. Swarm-technology for large-area photogrammetry survey and spatially complex 3D modeling. *Int. J. Latest Res. Eng. Technol.* **2018**, *4*, 33–39.
17. DJI Agriculture. DJI Agriculture Launches the Mavic 3 Multispectral Spark the Development of Precision Agriculture [Video]. Available online: <https://www.youtube.com/watch?v=WeDvNscRRPE> (accessed on 8 October 2023).
18. Geophysical Insights. PARADISE: The AI Workbench for Seismic Interpretation. Available online: <https://www.geoinsights.com/> (accessed on 3 September 2023).
19. Itten, J. *The Art of Color*; Gustavo Gili: Barcelona, Spain, 2020; Volume 1, pp. 1–136.
20. Heller, E. *Color Psychology: How Colors Affect Feelings and Reason*; Gustavo Gili: Barcelona, Spain, 2008; Volume 1, pp. 1–301. (In Spanish)
21. Stevens, E.; Antiga, L.; Viehmann, T. *Deep Learning with PyTorch*; Manning: Shelter Island, NY, USA, 2020; Volume 1, pp. 1–522.
22. Jack, K. *Video demystified: A Handbook for the Digital Engineer*; Elsevier: Amsterdam, The Netherlands, 2007; Volume 1, pp. 1–939.
23. Midjourney. Available online: <https://www.midjourney.com/home/?callbackUrl=/app/> (accessed on 16 October 2023).
24. Jaruga-Rozdolska, A. Artificial intelligence as part of future practices in the architect's work: MidJourney generative tool as part of a process of creating an architectural form. *Architectus* **2022**, *3*, 95–103. [CrossRef]
25. Chen, J.; Wang, D.; Shao, Z.; Zhang, X.; Ruan, M.; Li, H.; Li, J. Using AI to generate master-quality architectural designs from text descriptions. *Buildings* **2023**, *13*, 2285. [CrossRef]
26. Pech-Ricárdez, A.A. *Sunset After the Rain [Painting]*; Private collection: Oaxaca, Mexico, 2019.

27. Marfurt, K.J.; Kirilin, R.L.; Farmer, S.L.; Bahorich, M.S. 3-D seismic attributes using a semblance-based coherency algorithm. *Geophysics* **1998**, *63*, 1150–1165. [[CrossRef](#)]
28. Serrano.Academy. Clustering: K-means and Hierarchical [Video]. Available online: <https://www.youtube.com/watch?v=QXOkPvFM6NU> (accessed on 9 October 2023).
29. *NOM-018-ENER*; Thermal Insulators for Buildings. Characteristics and Test Methods. ENER: Mexico City, Mexico, 2011.
30. *NMX-C-228-ONNCCE*; Construction Industry—Thermal Insulating Materials—Determination of Moisture Adsorption and Water Absorption. ONNCCE: Mexico City, Mexico, 2010.
31. *NMX-C-037-ONNCCE*; Construction Industry—Masonry—Determination of Total Absorption and Initial Water Absorption in Blocks, Partitions, or Bricks and Large Bricks—Test Method. ONNCCE: Mexico City, Mexico, 2013.
32. *NMX-C-404-ONNCCE*; Construction Industry—Masonry—Blocks, Partitions, or Bricks and Large Bricks for Structural Use—Specifications and Test Methods. ONNCCE: Mexico City, Mexico, 2012.
33. Darnault, C.J.G.; Throop, J.A.; DiCarlo, D.A.; Rimmer, A.; Steenhuis, T.S.; Parlange, J.Y. Visualization by light transmission of oil and water contents in transient two-phase flow fields. *J. Contam. Hydrol.* **1998**, *31*, 337–348. [[CrossRef](#)]
34. Cuddy, S. Using fractals to determine a reservoir’s hydrocarbon distribution. In Proceedings of the 58th Annual Logging Symposium, Oklahoma City, OK, USA, 17–21 June 2017; Society of Petrophysicists and Well Log Analysts: Oklahoma City, OK, USA, 2017.
35. Huntley, H.E. *The Divine Proportion: A Study in Mathematical Beauty*; Dover: Mineola, NY, USA, 1970; Volume 1, pp. 1–186.
36. Cochrane, S. The Munsell Color System: A scientific compromise from the world of art. *Stud. Hist. Philos. Sci.* **2014**, *47*, 26–41. [[CrossRef](#)] [[PubMed](#)]
37. dos Santos, J.F.C.; Silva, H.R.F.; Pinto, F.A.C.; de Assis, I.R. Use of digital images to estimate soil moisture. *Rev. Bras. Eng. Agrícola E Ambient.* **2016**, *20*, 1051–1056. [[CrossRef](#)]
38. Liu, G.; Tian, S.; Xu, G.; Zhang, C.; Cai, M. Combination of effective color information and machine learning for rapid prediction of soil water content. *J. Rock Mech. Geotech. Eng.* **2023**, *15*, 2441–2457. [[CrossRef](#)]
39. Yoshimoto, N.; Orense, R.P.; Tanabe, F.; Kikkawa, N.; Hyodo, M.; Nakata, Y. Measurement of degree of saturation on model ground by digital image processing. *Soil Found.* **2011**, *51*, 167–177. [[CrossRef](#)]
40. Ogata, A.; Banks, R.E. *A Solution of the Differential Equation of Longitudinal Dispersion in Porous Media*; Geological Survey Professional, Paper 411-A; US Government Printing Office: Washington, DC, USA, 1961; pp. 1–7.
41. Bejan, A. *Heat Transfer*; John Wiley and Sons: New York, NY, USA, 1993; Volume 1, pp. 1–675.
42. Rangel-Germán, E.R. Water Infiltration in Fractured Porous Media: In-situ Imaging, Analytical Model, and Numerical Study. Ph.D. Thesis, Stanford University, Stanford, CA, USA, 2003; pp. 1–182.
43. Peeters, M.; Kovats, J.; Moita, C.; Pech, A.; Moulton, C.; Abraham, J. Monitoring and modeling invasion using ground penetrating radar and flow simulation programs. In Proceedings of the 43rd Annual Logging Symposium, Oiso, Japan, 2–5 June 2002; Society of Petrophysicists and Well Log Analysts: Oiso, Japan, 2002.
44. Kovats, J.A. Formation Invasion from a Horizontal Wellbore: Ground Penetrating Radar, Imaging, and Numerical Flow Simulations of a Physical Model. Master’s Thesis, Colorado School of Mines, Golden, CO, USA, 2001; pp. 1–212.
45. Hussaini, S.R.; Dvorkin, J. Specific surface area versus porosity from digital images: High-porosity granular samples. *J. Pet. Sci. Eng.* **2021**, *206*, 108961. [[CrossRef](#)]
46. Tempfli, K.; Kerle, N.; Huurneman, G.C.; Janssen, L.L.F. *Principles of Remote Sensing*; International Institute for Geo-information Science and Earth Observation: Enschede, The Netherlands, 2009; Volume 1, pp. 1–591.
47. Pirson, S.J. *Elements of Oil Reservoir Engineering*; McGraw-Hill: New York, NY, USA, 1950; Volume 1, pp. 1–441.
48. Wang, A.; Pollack, G.H. Exclusion-zone water inside and outside of plant xylem vessels 2024. *Nat. Sci. Rep.* **2024**, *14*, 12071.
49. Ahl, J. Salt diffusion in brick structures. *J. Mater. Sci.* **2003**, *38*, 2055–2061. [[CrossRef](#)]
50. Feynman, R.; Leighton, R.; Sands, M. *The Feynman Lectures on Physics*; California Institute of Technology: Reading, MA, USA, 1963; Volume 2, pp. 1–697.
51. Dais, D.; Bal, I.E.; Smyrou, E.; Sarhosis, V. Automatic crack classification and segmentation on masonry surfaces using convolutional neural networks and transfer learning. *Autom. Constr.* **2021**, *125*, 103606. [[CrossRef](#)]
52. Gradišar, L.; Dolenc, M. Transfer and Unsupervised Learning: An Integrated Approach to Concrete Crack Image Analysis. *Sustainability* **2023**, *15*, 3653. [[CrossRef](#)]
53. Baduge, S.K.; Thilakarathna, S.; Perera, J.S.; Arashpour, M.; Sharafi, P.; Teodosio, B.; Shringi, A.; Mandis, P. Artificial intelligence and smart vision for building and construction 4.0: Machine and deep learning methods and applications. *Autom. Constr.* **2022**, *141*, 104440. [[CrossRef](#)]
54. Bazán-González, G. Digital transformation in the construction industry. Driven by the professional use of drones. *Mex. Mag. Constr.* **2021**, *647*, 70–73. (In Spanish)
55. DRONE INDUSTRY INSIGHTS. *Drone Market Size, Forecast 2022–2026, Market Developments and Regulations*; DRONE INDUSTRY INSIGHTS: Hamburg, Germany, 2022.

56. Khorrani, M.; Shirzaei, M.; Ghobadi-Far, K.; Werth, S.; Carlson, G.; Zhai, G. Groundwater Volume Loss in Mexico City Constrained by InSAR and GRACE Observations and Mechanical Models. *Geophys. Res. Lett.* **2023**, *50*, e2022GL101962. [[CrossRef](#)]
57. Hughes, R.E.; Bargh, B.L. *The Weathering of Brick: Causes, Assessment and Measurement. A Report of the Joint Agreement Between the U.S. Geological Survey and the Illinois State Geological Survey*; US Geological Survey: Reston, VA, USA, 1982; Volume 1, pp. 1–92.
58. Rahaman, M.N. *Sintering of Ceramics*; CRC Press: Boca Raton, FL, USA, 2007; Volume 1, pp. 1–875.
59. Qin, Z.; Jung, G.S.; Kang, M.J.; Buehler, M.J. The mechanics and design of a lightweight three-dimensional graphene assembly. *Sci. Adv.* **2017**, *3*, e1601536. [[CrossRef](#)] [[PubMed](#)]
60. Anwajler, B. The thermal properties of a prototype insulation with a gyroid structure—Optimization of the structure of a cellular composite made using SLS printing technology. *Materials* **2022**, *15*, 1352. [[CrossRef](#)]
61. Iberdrola. Bioclimatic Architecture, Constructions That Respect the Environment. Available online: <https://www.iberdrola.com/innovacion/que-es-arquitectura-bioclimatica> (accessed on 30 October 2023). (In Spanish).
62. Requena-Ruiz, I. Bioclimatism in the architecture of Le Corbusier: The Palace of the Spinners. *Constr. Rep.* **2012**, *64*, 549–562. (In Spanish)
63. Shen, Z.; Yang, Y.; Fu, X.; Adams, K.H.; Biondi, E.; Zhan, Z. Fiber-optic seismic sensing of vadose zone soil moisture dynamics. *Nat. Commun.* **2024**, *15*, 6432. [[CrossRef](#)]
64. Ricárdez-Montiel, A.A. Estimation of moisture percentage in fired red brick using digital image processing. Bachelor's Degree Thesis, Universidad Autónoma Benito Juárez de Oaxaca, Oaxaca, Mexico, 2024; pp. 1–125. (In Spanish).

**Disclaimer/Publisher's Note:** The statements, opinions and data contained in all publications are solely those of the individual author(s) and contributor(s) and not of MDPI and/or the editor(s). MDPI and/or the editor(s) disclaim responsibility for any injury to people or property resulting from any ideas, methods, instructions or products referred to in the content.